

Subject-driven Video Generation via Disentangled Identity and Motion

Daneul Kim^{1,3,§} Jingxu Zhang^{3,§} Wonjoon Jin^{2,§} Sunghyun Cho² Qi Dai³ Jaesik Park¹ Chong Luo³

¹Seoul National University

²POSTECH

³Microsoft Research Asia



Figure 1. **Main results.** Our method produces high-quality subject-driven video generation (SDV-Gen) in a zero-shot manner. We extend video generative models to have SDV-Gen capability using the small datasets. For the first two rows, we fine-tune CogVideoX-5B with 4,000 unpaired video set and 200K paired subject-image set. For the result in the last row, we use only 4,000 unpaired videos and 4,000 paired subject-images.

Abstract

Subject-driven video generation (SDV-Gen) aims to produce videos of a specific subject by fine-tuning a pretrained video model, enabling a wide range of personalized and application-driven use cases. However, its practical deployment remains challenging. Zero-shot methods achieve generalization without any requirement for per-subject tuning but demand prohibitive resources for fine-tuning phase, relying on millions of paired subject-videos and 10K–200K A100 GPU hours for fine-tuning. Per-subject tuning methods, such as CustomCrafter, avoid large-scale fine-tuning but require approximately 200 A100 hours of fine-tuning per subject at test-time, thereby limiting practicality. To address these challenges, we introduce a novel zero-shot SDV-Gen framework that dramatically reduces both data and training requirements while eliminating per-subject tuning at infer-

ence. Our framework decomposes SDV-Gen into (i) identity injection from paired subject-images and (ii) motion-awareness preservation from unpaired videos. A stochastic schedule alternates between these objectives by randomly sampling frames and dropping image tokens to avoid trivial solutions. Gradient analysis shows that these objectives update independent parameter subspaces, explaining why separating them into two tasks enables stable joint optimization without interference. Our zero-shot method adapts CogVideoX-5B using only 200K paired subject-images and 4,000 unpaired videos (1% of Pexels-400K) in 288 A100 GPU hours, which is 35–730× faster than zero-shot baselines, demonstrating competitive motion quality and subject fidelity to the heavily resourced approaches.

1. Introduction

Recent advances in video diffusion models [4, 20, 49, 54] have expanded controllable text-to-video (T2V) synthesis

[§]Work done during internship at Microsoft Research Asia.

Table 1. **Dataset and computation comparison between zero-shot and per-subject tuning Subject-driven Video Generation methods along with zero-shot capabilities.** We compare per-subject tuning methods’ required inputs and per-subject tuning time along with zero-shot methods’ dataset size and required finetuning time.

<i>Per-subject Tuning Methods</i>	Required Inputs	Base Model (Param.)	Tuning Steps	A100 hours*	Zero-shot
CustomCrafter [53]	200 regularizing images per subject	VideoCrafter2 [8] (1.4B)	10K	200 [‡]	✗
Still-Moving [7]	Few reference images + 40 videos	Lumiere [3] (1.2B)	500	–	✗
<i>Zero-shot Methods</i>	Dataset Size	Base Model (Param.)	Train Steps	A100 hours*	Zero-shot
VideoBooth [26]	48,724 subject-video pairs	Stable Diffusion-based VDM [19, 40] (1.08B)	400K [‡]	775–1,938 [‡]	△
VACE [27]	53M video [†] pairs	LTX [17] & Wan [49] (1.3–14B)	200K	70K–210K [‡]	✓
Phantom [33]	1M subject-video pairs	Wan [49] (1.3–14B) + Seed [47]	30K	10K–30K [‡]	✓
Ours	200K paired subject-image sets + 4,000 unpaired videos	CogVideoX (5B)	4,000	288	✓

[†]Source video pool. ^{*}Total GPU hours. [‡]Estimated from reported batch sizes and wall-clock training time. Please see the supplement for details.

and video customization, enabling conditioning on signals such as keypoints, edges, and reference images [1, 23, 31, 44, 55]. Building on this progress, *subject-driven video generation* [24, 26, 50, 51, 57, 62] (also known as subject-to-video customization or video personalization, *i.e.*, SDV-Gen) seeks to synthesize videos that preserve a target subject’s identity while allowing variations in scene, motion, and context, an ability essential for personalized content creation. In practice, this is typically achieved by adapting a pretrained T2V backbone to the target subject.

Early SDV-Gen approaches fine-tune a separate model or LoRA per subject [7, 41, 50, 53], limiting scalability, while more recent methods train a single model that generalizes to unseen subjects [11, 22, 24, 26, 27, 33, 57]. Yet these zero-shot methods still rely on large paired subject-video datasets and massive computation (Table 1; 10^4 – 10^5 A100 GPU-hours for VACE and Phantom [27, 33]). This implicitly assumes that both identity and motion-awareness must be learned from paired subject-videos, motivating the question: *to what extent does subject-driven video generation actually require paired subject-videos?*

A potential alternative is to learn identity from subject-driven image generation (SDI-Gen) data (*i.e.*, paired subject-images) while inheriting motion priors from the pretrained T2V backbone. In principle, paired subject-images provide strong identity cues, whereas the backbone encodes motion priors (*i.e.*, temporal dynamics) from large-scale pretraining. However, naïve fine-tuning on paired subject-images severely degrades inter-frame temporal coherence, often causing motion to collapse into inconsistent dynamics or near-static (“frozen”) movement. This suggests that identity and motion modeling interfere with each other when optimized sequentially, indicating that treating SDV-Gen as a single objective may be fundamentally limiting.

In this work, we propose a zero-shot SDV-Gen method that decomposes the subject-driven video generation into two complementary components: identity injection from paired subject-images and motion-awareness preservation from a small set of unpaired videos. A stochastic task-

switching schedule alternates between these objectives, predominantly sampling paired subject-images while using unpaired videos only to maintain temporal coherence. Interestingly, this formulation allows identity and motion to be learned from different data sources, avoiding the collapse observed in naïve SDI-Gen fine-tuning and eliminating the need for paired subject-videos.

To understand why joint optimization is stable, we analyze the gradients of the two objectives. We observe that gradient conflict of the two objectives diminishes rapidly and become nearly orthogonal during the fine-tuning, indicating that identity and motion update independent parameter subspaces. This provides a mechanistic explanation for why dual-task learning avoids interference and why large-scale paired subject-videos are not strictly necessary.

This leads to a data- and compute-efficient, zero-shot (*i.e.*, tuning-free at test time) framework. We adapt CogVideoX-5B on 200K subject-image pairs and only 4,000 unpaired videos (1% of Pexels-400K) [29] and train within 288 A100-hours. We further show that the method remains effective even with just 4,000 paired subject-images (50× fewer pairs). Despite this modest budget and without any paired subject-videos, our single model generalizes to unseen subjects in a zero-shot manner and achieves competitive quality against substantially more expensive zero-shot and per-subject tuning baselines.

Our contributions are in threefold:

- We introduce a zero-shot subject-driven video generation framework that separates identity injection from motion preservation, enabling training without any paired subject-videos.
- We provide a gradient analysis showing that the identity and motion-aware objectives update independent parameter subspaces, explaining why the proposed formulation remains stable without paired subject-videos.
- We demonstrate zero-shot subject-driven video generation using only 200K paired subject-images and 4,000 unpaired videos, achieving competitive quality trained in 288 A100-hours.

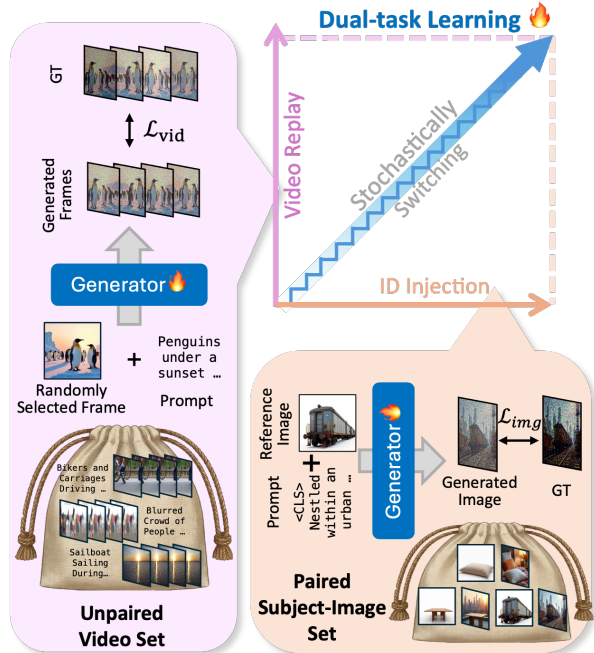


Figure 2. **Dual-task learning strategy.** We formulate subject-driven video generation as a *dual-task* problem. First is identity injection (Bottom) from paired subject-images, and second is motion-awareness preservation (Left), which we utilize unpaired videos and conduct stochastically switched learning.

2. Related Work

2.1. Subject-driven Image Generation

Diffusion models have greatly advanced text-to-image generation [10, 14, 40], and many works focus on injecting novel subjects while preserving identity. Early methods add spatial control such as poses or edges [37, 60], while later cross-attention-based encoders such as IP-Adapter and SSR-Encoder [55, 61] and personalization methods including DreamBooth, Textual Inversion, CustomDiffusion, DisenBooth, and recent multi-subject or zero-shot schemes [5, 9, 13, 16, 30, 34, 41, 46, 48, 59] learn subject-specific representations from paired subject-images for SDI-Gen. We follow this line by reusing a paired subject-images (Subject-200K from OmniControl [44]) as our main identity supervision, but explicitly utilize a small amount of unpaired videos to handle temporal coherence.

2.2. Subject-driven Video Generation

SDV-Gen extends SDI-Gen to the temporal domain. Per-subject tuning methods such as DreamVideo, MotionBooth, Still-Moving, and CustomCrafter [7, 50, 52, 53] fine-tune a model or LoRA for each identity, while zero-shot approaches like VideoBooth, Concept-Master, DreamVideo-2, MagicMirror, ID-Animator, and Consis-ID [18, 24, 26, 51, 57, 62] train a single zero-shot model but still rely on

paired subject-videos and often target restricted domains (e.g., faces). Large-scale DiT-based systems such as VACE, Phantom, HunyuanCustom, and VideoAlchemist [11, 22, 27, 33] further improve quality by training on million-scale datasets such as Phantom-Data and OpenS2V-Nexus [12, 58], at the cost of 10^4 to 10^5 A100-hours. In contrast, we adapt a pretrained CogVideoX-5B [54] backbone to zero-shot SDV-Gen using 200K paired subject-images and only a few thousand unpaired videos (about 1% of Pexels-400K [29]) for efficient SDV-Gen without expensive training or data, as summarized in Table 1.

2.3. Multi-task Optimization

Our method optimizes two objectives on a single model: an identity injection loss on SDI-Gen data and a motion-aware loss on unpaired videos, placing it in the context of multi-task learning, where conflicting gradients across tasks can hurt performance and gradient-surgery methods such as PCGrad [56] explicitly modify updates to reduce interference. Continual-learning and replay techniques [6, 15, 35, 36, 39, 42] also mitigate forgetting by revisiting past samples or synthetic memories. In contrast, we use a fixed set of unpaired videos and a simple stochastic task-switching scheme between SDI-Gen data and image-to-video (I2V) updates, and we analyze the resulting gradients rather than enforcing explicit projections or maintaining a growing memory.

3. Method

3.1. Preliminaries

We fine-tune a pretrained multi-modal diffusion transformer (MM-DiT) [38] for subject-driven video generation. We adopt CogVideoX-5B [54] as our backbone, which provides strong text-video alignment and motion priors from large-scale pretraining. Building on this, we briefly revisit the MM-DiT formulation and then describe how we inject subject-driven image-generation priors while preserving motion dynamics using a small set of unpaired videos.

At each denoising step, MM-DiT processes noisy visual tokens $X \in \mathbb{R}^{N \times d}$ and text tokens $C_T \in \mathbb{R}^{M \times d}$ that share embedding dimension d . Each block consists of LayerNorm followed by multi-modal attention (MMA) over the concatenated sequence $[X; C_T]$: $\text{MMA}([X; C_T]) = \text{softmax}\left(\frac{QK^T}{\sqrt{d}}\right)V$, where Q, K, V are the usual query, key, and value projections. Spatial and temporal positions are encoded with RoPE [43], applied to visual tokens as $X_{i,j} \leftarrow X_{i,j} \cdot R(i, j)$.

Because attention costs scale quadratically with the number of tokens, fine-tuning solely on large video datasets is substantially more expensive than image-only training. Our goal is to adapt this backbone for SDV-Gen using subject-image pairs predominantly, plus a small set of unpaired

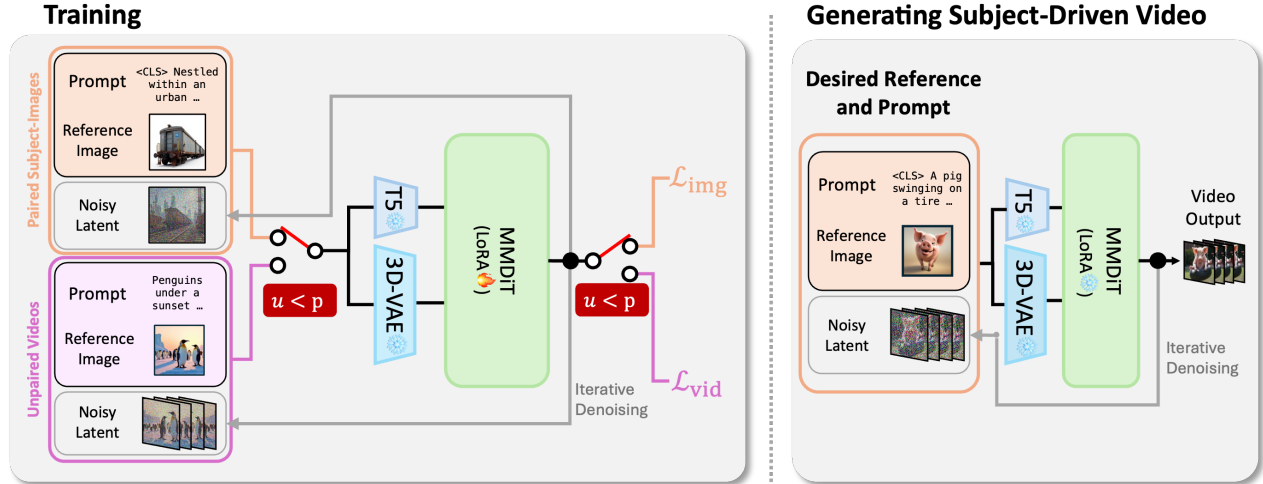


Figure 3. **Training and Inference Details.** **Left:** During training, we stochastically alternate between two objectives: identity injection using paired subject-images and motion-awareness preservation using a small set of unpaired videos. **Right:** At inference time, *no additional per-subject tuning is required*. The model generates a video conditioned on the reference image and text prompt in a zero-shot manner.

videos.

3.2. Dual-Task Formulation

We formulate SDV-Gen as a dual-task problem as in Fig. 2:

(i) **identity injection** from subject-images pairs to learn subject appearance, and (ii) **motion-awareness** from unpaired videos.

Let \mathcal{D}_{img} denote a dataset of paired subject-image tuples $\{(I_{\text{ref}}, I_{\text{out}}, P)\}$, where I_{ref} and I_{out} depict the same subject under different poses, viewpoints, or contexts, and P is the text prompt. Let \mathcal{D}_{vid} denote an unpaired text-video dataset $\{(T, V)\}$, where T is the text prompt and V is the corresponding video. We define two diffusion objectives, $\mathcal{L}_{\text{img}} = \mathcal{L}_{\text{subject-image}}(I_{\text{ref}}, I_{\text{out}}, P)$ and $\mathcal{L}_{\text{vid}} = \mathcal{L}_{\text{text-video}}(T, V)$, with gradients $g_{\text{img}} = \nabla_{\theta} \mathcal{L}_{\text{img}}$ and $g_{\text{vid}} = \nabla_{\theta} \mathcal{L}_{\text{vid}}$ with respect to the trainable parameters θ .

We optimize via stochastic task-switching (Fig. 3): at each iteration, draw $u \sim \mathcal{U}(0, 1)$ and select

$$\mathcal{L}_{\text{total}} = \begin{cases} \mathcal{L}_{\text{vid}}, & \text{if } u < p, \\ \mathcal{L}_{\text{img}}, & \text{otherwise,} \end{cases} \quad (1)$$

yielding expected update $\mathbb{E}[g] = (1 - p)g_{\text{img}} + pg_{\text{vid}}$. We use $p = 0.2$, so 80% of updates come from paired subject-images and 20% from unpaired videos during the fine-tuning.

3.3. Identity Injection with Paired Subject-Images

Following OminiControl [44], given subject-image pairs $(I_{\text{ref}}, I_{\text{out}})$ of the same subject and prompt P , we encode $X_{\text{ref}} = \text{VAE}(I_{\text{ref}})$, $X_{\text{out}} = \text{VAE}(I_{\text{out}})$, $C_T = \text{T5}(P)$, and train MM-DiT for X_{out} conditioned on (X_{ref}, C_T) . For single-frame input, we truncate RoPE embeddings to match the token count of one frame.

We apply LoRA [21] to a subset of attention and normalization layers that interact with reference-image tokens; the rest of the backbone remains frozen. To anchor subject identity in the text stream, we prepend a special $\langle \text{CLS} \rangle$ token to prompts (e.g., “An $\langle \text{CLS} \rangle$ armchair in the living room”). Ablations in the supplement confirm that $\langle \text{CLS} \rangle$ improves identity metrics (CLIP-I, DINO-I) without degrading motion quality.

3.4. Motion Awareness with Unpaired Videos

Fine-tuning with SDI-Gen data on pre-trained video model tends to erode temporal modeling, producing videos that are nearly static at test time, with little to no motion. To preserve motion, we introduce an image-to-video (I2V) objective on a small set of unpaired videos of $(T, V) \in \mathcal{D}_{\text{vid}}$. For each video, we sample a reference frame index i and set $I_{\text{ref}} = V_i$ as conditioning, while the full video V serves as the reconstruction target. We encode

$$X_{\text{ref}} = \text{VAE}(I_{\text{ref}}), \quad X_{\text{vid}} = \text{VAE}(V), \quad C_T^{\text{vid}} = \text{T5}(T), \quad (2)$$

and train MM-DiT for X_{vid} conditioned on $(X_{\text{ref}}, C_T^{\text{vid}})$. We adopt I2V training scheme rather than T2V training since it matches the inference-time modality (reference image \rightarrow video) and decouples identity injection from motion dynamics.

Mitigating First-frame Copying. Conditioning on the first frame of a video from unpaired videos can cause the model to simply copy it with minimal motion, since distinguishing subject with the background is required for SDV-Gen compared to I2V. Therefore, we apply two regularizers: (i) *random frame selection*, instead of using the first frame of a given video, we sample i randomly from $\{1, \dots, T\}$ rather

than fixing to the first frame. (ii) *image-token dropping*, instead of using the I2V fine-tuning scheme fully, we randomly drop image tokens from X_{ref} with probability p_{drop} to encourage the model to infer motion rather than copy. Please refer to supplement for the explanation on reduced static artifacts when applying regularizers.

3.5. Training Procedure

Putting everything together, fine-tuning proceeds as follows. At each training step we sample $u \sim \mathcal{U}(0, 1)$ and

1. if $u < p$, draw a mini-batch of videos (T, V) from \mathcal{D}_{vid} , sample a random reference frame and apply image-token dropping, and update θ with $\mathcal{L}_{\text{vid}}(T, V)$;
2. otherwise, draw paired subject-images $(I^{(1)}, I^{(2)}, P)$ from \mathcal{D}_{img} and update θ with $\mathcal{L}_{\text{img}}(I^{(1)}, I^{(2)}, P)$.

This stochastic proxy replay maintains motion-awareness through occasional video updates while injecting identity from paired subject-image in most steps.

SDI-Gen→I2V. A straightforward alternative is to generate a subject image with an SDI-Gen model and then apply a pre-trained I2V model. However, this pipeline relies on clear subject visibility in the initial frame for identity propagation, which often fails in dynamic scenes (e.g., “a toy car comes closer to the camera on a wet pavement,” Figure 4). When the subject is small or occluded, the image-to-video model may misidentify it and introduce inconsistent or fabricated details, causing a *progressive loss of identity* in later frames.

Compute Efficiency. Let C_{img} and C_{vid} denote the per-step cost of SDI-Gen and I2V updates. Under MM-DiT attention, video tokens for T latent frames incur roughly T^2 times the cost of images; for $T = 13$ we observe $C_{\text{vid}} \approx 169 C_{\text{img}}$. With a replay ratio $p = 0.2$, the expected cost per step is

$$\begin{aligned} \mathbb{E}[C] &= (1 - p)C_{\text{img}} + pC_{\text{vid}} \\ &\approx 0.8C_{\text{img}} + 0.2 \cdot 169C_{\text{img}} \approx 34.6 C_{\text{img}}, \end{aligned} \quad (3)$$

which is *much lower than fine-tuning on videos alone*. Using only 4,000 unpaired videos ($\sim 1\%$ of Pexels-400K) yields 288 A100-hours while achieving competitive zero-shot SDV-Gen performance (Table 1).

4. Gradient Dynamics in Dual-Task Learning

In Sec. 3.2 we formulated SDV-Gen as a dual-task learning problem with two losses $(\mathcal{L}_{\text{img}}, \mathcal{L}_{\text{vid}}$, with gradients $g_{\text{img}}(t)$ and $g_{\text{vid}}(t)$. To analyze the gradient dynamics, we freeze the model at each checkpoint θ_t , and compute $g_{\text{img}}(t)$ and $g_{\text{vid}}(t)$ on mini-batches from \mathcal{D}_{img} and \mathcal{D}_{vid} w.r.t. the trainable parameters θ_{train} (LoRA and task-specific normalization layers) as in training, and log their cosine similarity $\phi(t)$ together with the gradient norms $\|g_{\text{img}}(t)\|_2$ and $\|g_{\text{vid}}(t)\|_2$. We provide the detailed measurement protocols in the supplement.



Figure 4. **Limitation of SDI-Gen→I2V method.** With the subject presented small in the first frame, I2V fails to generate consistent results as it cannot interpret low-resolution subjects.

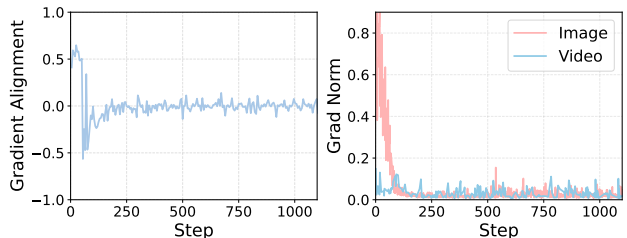


Figure 5. **Gradient analysis on alignment and norms during fine-tuning.** **Left:** Cosine similarity $\phi(t)$ between g_{img} and g_{vid} (over trainable parameters) quickly collapses to a narrow band near zero under dual-task training, indicating emergent near-orthogonality. **Right:** ℓ_2 norms $\|g_{\text{img}}(t)\|_2$ and $\|g_{\text{vid}}(t)\|_2$ remain non-negligible and similar in scale after 100-step.

4.1. Do the Gradients Become Orthogonal?

Figure 5 plots the evolution of $\phi(t)$ under our stochastic dual-task learning. We fine-tune the pre-trained CogVideoX-5B using Subject-200K [44], which is a paired subject-image set and with unpaired video set [29]. Starting from initialization, the cosine rapidly converges to a narrow band around zero and remains there for the rest of the fine-tuning. This behavior is consistent with the hypothesis that, after a short transient, identity injection and motion-awareness preservation occupy nearly orthogonal directions in the parameter space of the trained model.

To rule out the trivial explanation that $\phi(t)$ appears close to zero only because both gradients vanish as the model converges, we additionally track the gradient norms. As shown in Fig. 5, both $\|g_{\text{img}}(t)\|_2$ and $\|g_{\text{vid}}(t)\|_2$ remain well above the numerical noise floor throughout fine-tuning. They stay within the same order of magnitude after initial drop in magnitude in $\|g_{\text{img}}(t)\|_2$. The decay of $\phi(t)$ therefore reflects a genuine change in the *direction* of the gradients rather than an artifact of vanishing magnitudes.

4.2. Gradient Convergence

The empirical behavior above suggests that stochastic switching between \mathcal{L}_{img} and \mathcal{L}_{vid} tends to reduce their gradient inner product. To provide some intuition, a proof in a

Table 2. Quantitative comparison with other methods on VBench. Note that we utilize publicly available version for Phantom [33] and VACE [27] based on Wan-2.1 1.3B [49].

<i>SDI-Gen</i> \rightarrow <i>I2V methods</i>	Motion Smooth.	Dynamic Degree	CLIP-T	CLIP-I	DINO-I
OminiControl [44]	98.21	51.67	31.89	72.58	54.16
BLIP [31]	97.53	49.17	28.19	79.29	56.58
IP-Adapter [55]	97.21	55.83	26.97	73.86	45.18
<i>SDV-Gen Methods</i>	Motion Smooth.	Dynamic Degree	CLIP-T	CLIP-I	DINO-I
VideoBooth [26]	96.95	51.67	29.59	66.06	34.54
Phantom [33]	98.93	54.90	33.51	72.49	51.94
VACE [27]	98.68	40.0	33.60	73.35	52.68
Ours	98.45	69.64	32.69	77.14	62.88

simplified setting (in a local second-order/quadratic model) is provided in the supplement (Appendix C).

Proposition 4.1 (Convergence of gradient inner product). *Consider two loss functions \mathcal{L}_1 and \mathcal{L}_2 that are L -smooth and locally convex in a neighborhood of convergence, and the stochastic update rule*

$$\theta_{t+1} = \theta_t - \eta g_t, \quad g_t = \begin{cases} \nabla \mathcal{L}_1(\theta_t), & \text{w.p. } 1-p, \\ \nabla \mathcal{L}_2(\theta_t), & \text{w.p. } p, \end{cases} \quad (4)$$

with a sufficiently small step size η . If the initial gradients exhibit non-trivial conflict, i.e., $\langle \nabla \mathcal{L}_1(\theta_0), \nabla \mathcal{L}_2(\theta_0) \rangle \neq 0$, then under the above assumptions the expected gradient inner product $\mathbb{E}[\langle \nabla \mathcal{L}_1(\theta_t), \nabla \mathcal{L}_2(\theta_t) \rangle]$ converges toward zero as t increases.

4.3. Relation to Gradient-Surgery Method

Several works in multi-task learning explicitly manipulate gradients to resolve conflicts, such as PCGrad [56], which projects each task gradient onto the normal plane of conflicting gradients. In our two-task setting, PCGrad would replace g_{img} by

$$g_{\text{img}}^{\text{PC}} = \begin{cases} g_{\text{img}} - \frac{\langle g_{\text{img}}, g_{\text{vid}} \rangle}{\|g_{\text{vid}}\|_2^2} g_{\text{vid}}, & \text{if } \langle g_{\text{img}}, g_{\text{vid}} \rangle < 0, \\ g_{\text{img}}, & \text{otherwise,} \end{cases} \quad (5)$$

and analogously for g_{vid} . This guarantees $\langle g_{\text{img}}^{\text{PC}}, g_{\text{vid}} \rangle \geq 0$ at each step, but requires computing *both* gradients and performing additional projections at every iteration, roughly doubling the cost compared to sampling a single task.

Our empirical analysis shows that the simpler stochastic switching scheme drives the gradient cosine $\phi(t)$ toward zero while keeping both norms non-vanishing, achieving a similar end effect as PCGrad but without explicit projections or extra gradient evaluations. For this reason, we use dual-task learning with stochastic switching as our default and regard PCGrad-style techniques as an interesting but unnecessary refinement in this setting. We provide details and gradient analysis for PCGrad in the supplement.

Table 3. Ablation result on training strategy of alternating optimization with image-only and two-stage fine-tuning approaches.

Training Method	Motion Smoothness	Dynamic Degree	CLIP-T	CLIP-I	DINO-I
Image-only	99.60	0.84	32.67	71.15	43.19
Two-stage	96.04	81.51	28.96	84.73	76.13
Ours	98.45	69.64	32.69	77.14	62.88

5. Experiments

5.1. Setup

Implementation. We build our approach on CogVideoX-5B, which adopts a 3D MM-DiT backbone [54], trained with a DDIM scheduler [40]. Joint fine-tuning of the two tasks is performed using AdamW with a learning rate of 5×10^{-5} and a cosine-with-restarts schedule. We fine-tune the CogVideoX-5B for 4,000 steps (~ 288 A100 GPU hours) using BF16 mixed precision, with batch sizes of 256 for images and 32 for videos. We apply LoRA (rank 128, dropout 0.1) to the designated trainable layers and use stochastic switching with probability $p = 0.2$.

We use OminiControl’s Subject200K dataset as our paired subject-image set. To study data efficiency, we additionally evaluate 2,000 and 4,000 subsets of Subject200K. We sample $\sim 4,000$ unpaired videos (1% of Pexels 400K), providing diverse real-world motion patterns. We train two sampling-rate variants: an 8 FPS model aligned with the original CogVideoX setting, and a 16 FPS model further trained on Pexels videos to improve motion smoothness and temporal consistency at higher frame rates. All ablations are conducted on CogVideoX, with additional implementation details deferred to the supplementary material.

Baseline. For zero-shot baselines, we use the SDV-Gen models of VideoBooth [26], Phantom [33] and VACE [27] with Wan 2.1-1.3B and additionally compare with state-of-the-art SDI-Gen models OminiControl [44], BLIP-Diffusion [31], and IP-Adapter [55], combined with the CogVideoX-5B I2V model: each first performs subject-driven image generation with its original setup, and we then generate videos via CogVideoX-5B. For per-subject tuning,

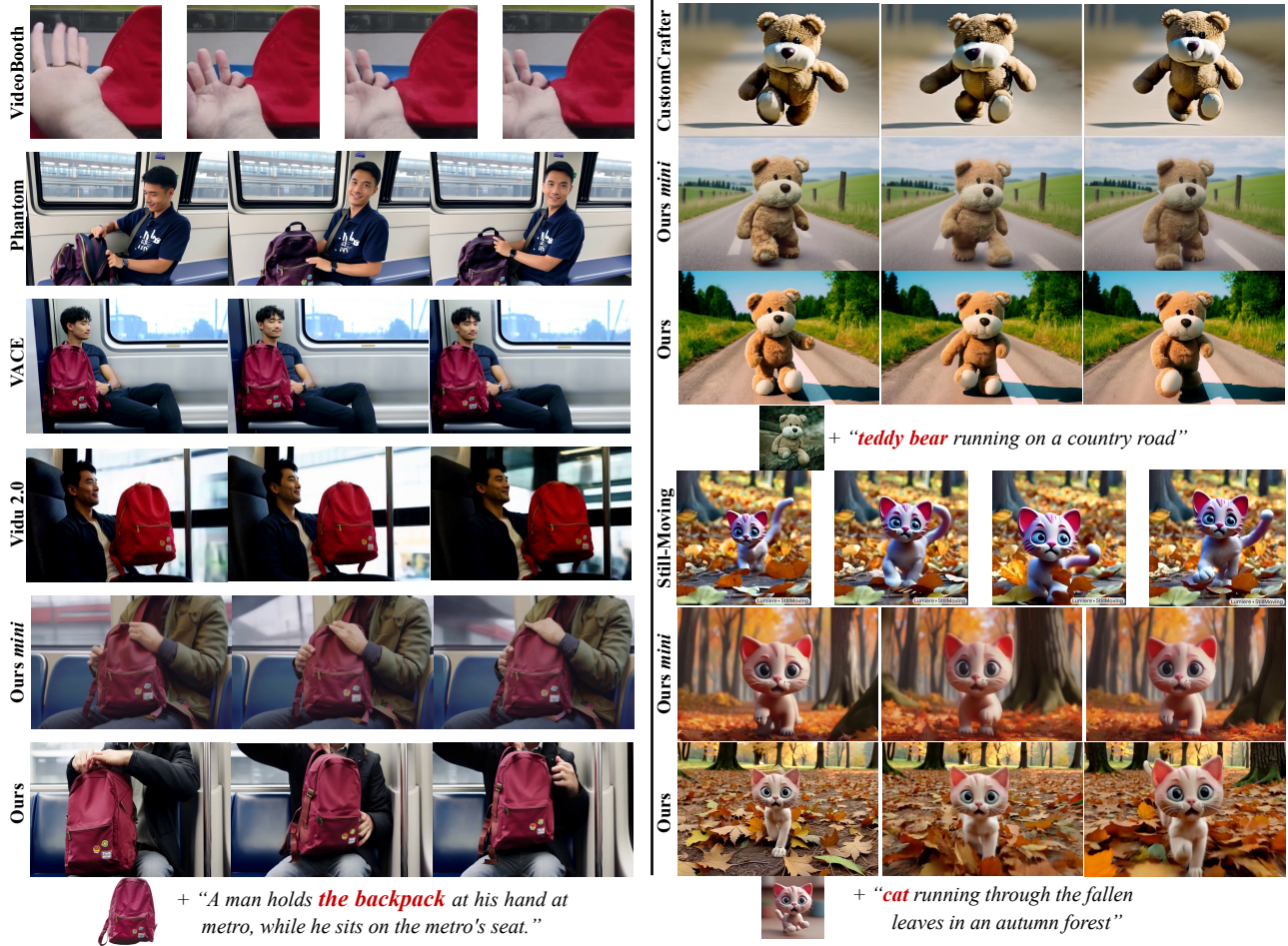


Figure 6. **Qualitative comparison with zero-shot methods (left) and per-subject tuning methods (right).** Ours *mini* denotes our model fine-tuned with 4,000 subset of Subject-200K [44]. Note that ours is zero-shot tuning-free, requiring no tuning at inference time.

we add qualitative comparison with Still-Moving [7] and CustomCrafter [53], using the results reported in their paper and supplements due to unavailable code or costly per-subject fine-tuning.

Evaluation Details. We randomly picked 30 reference images from state-of-the-art SDI-Gen sets [2, 7] and the traditional DreamBooth dataset [41]. We utilize GPT to generate 4 prompts for each image comprising of a total 120 pairs for video generation. Utilizing 120 videos, we report VBench metrics [25]: *Motion Smoothness* (temporal consistency), *Dynamic Degree* (amount of motion), *CLIP-T* (text-video alignment), *CLIP-I* (CLIP-based image similarity), and *DINO-I* (DINO-based subject fidelity). Also note that we additionally provide OpenS2V evaluation benchmark result in the supplement.

5.2. Comparison with Baselines

Quantitative Analysis. Table 2 shows our method outperforming all baselines in zero-shot SDV-Gen, achieving the highest dynamic degree (69.64) and identity consistency

Table 4. Ablation on the number of Subject200K paired subject-images. Using only 2,000 or 4,000 pairs achieves performance comparable to fine-tuning with the full 200K pairs.

Training Method	# of Paired Subject-Images	Motion Smoothness	Dynamic Degree	CLIP-T	CLIP-I	DINO-I
Ours-tiny	2,000	98.72	60.71	33.38	74.72	57.03
Ours-mini	4,000	97.99	78.33	33.22	75.87	58.86
Ours	200K	98.45	69.64	32.69	77.14	62.88

ency (DINO-I, 62.88), while maintaining strong motion smoothness (98.45) and text alignment (CLIP-T, 32.69). Compared to recent SDV-Gen methods such as Phantom and VACE, our approach yields competitive dynamics and identity scores even with much less training time and data. Among SDI-Gen→I2V based pipelines (OminiControl+I2V, BLIP+I2V, IP-Adapter+I2V), BLIP+I2V attains the highest CLIP-I (79.29), but with weaker dynamics and DINO-I; our method offers a more balanced trade-off between motion and subject fidelity.

Qualitative Analysis. As illustrated on the left of Fig 6,



Figure 7. **Qualitative Comparison with PCGrad.**

our method demonstrates better detail, ID consistency, and motion-awareness than tuning-free baselines Vidu 2.0 and VideoBooth, and is competitive with Phantom and VACE with Wan. For the backpack example, our model faithfully reproduces fine textures and foreground motion, whereas Vidu 2.0 preserves ID but exhibits jittery trajectories, and VideoBooth yields the weakest identity fidelity. Our approach preserves identity under diverse motions, matching the quantitative gains observed in Tab 2.

We show qualitative comparisons with CustomCrafter [53] and Still-Moving [7] using their official samples in Fig 6 (right). Our results in rows 2,3 and row 5,6 remain more identity-faithful, whereas CustomCrafter often exhibits distorted or drifting details, with Still-Moving [7] neglects details such as whiskers. Also note that ours *mini*, fine-tuned only with 4,000 pairs of SDI-Gen data, also demonstrates competitive quality to baselines.

5.3. Ablation Study

Training Strategy. We compare *image-only*, *two-stage*, and our *dual-task* training strategies. Image-only fine-tuning produced high motion smoothness (99.60) because static videos (0.84 dynamic degree) lead to smooth motion, indicating a need for improved dynamics. (Tab. 3) Two-stage fine-tuning improved dynamics (81.51) and similarity (CLIP-I: 84.73) but introduced severe artifacts and identity forgetting. Our *dual-task learning* excelled, balancing motion smoothness (98.72) and dynamic degree (60.19).

Comparison with PCGrad. We also apply PCGrad [56] on top of our dual-task learning, but observe only minor visual differences compared to our default stochastic switching (Fig. 7). Given the similar performance but roughly doubled gradient computation, we adopt the simpler stochastic schedule as our default and regard PCGrad as an optional refinement. We also provide comparisons in the supplement.

Different Sizes of Image Datasets. As shown in Figure 1 and Table 4, our method remains robust even when the number of paired subject-images is reduced from 200K to 4,000 (Ours *mini*) or 2,000 (Ours *tiny*): dynamic degree and motion smoothness stay high, and identity metrics (CLIP-I,



Figure 8. **Human Face-driven Video Generation.** Demonstration of successful cases and failure cases on human face-driven generation.

DINO-I) degrade only moderately. This suggests that the benefit of identity injection can be obtained from a relatively small set.

5.4. Limitations

Our primary fine-tuning dataset, Subject-200K [44], primarily comprises general objects and contains almost no human faces. Despite this, our model generalizes reasonably well to certain human faces, as shown in the first row of Figure 8. However, as shown in the second row, some results exhibit blurry artifacts and fail to preserve nuanced identity features. We believe incorporating an identity-focused dataset would mitigate this issue.

Additionally, the dataset predominantly contains spatially-centered objects, limiting our model’s ability to place subjects at arbitrary locations within frames, since Subject-200K is synthesized using FLUX. Finally, our theoretical analysis in Section 4 relies on simplifying assumptions that may not fully capture the behavior of deep nonlinear networks and we leave a more rigorous treatment for future work.

6. Conclusion

We recast subject-driven video generation as a dual-task problem that combines identity injection from paired subject-images with motion-awareness from a small set of unpaired videos. Using a simple stochastic task-switching scheme, our method replaces expensive paired subject-videos with 200K paired subject-images and 4,000 unpaired videos (which is only 288 A100-hours in total), while still generalizing to unseen subjects in a zero-shot manner. Gradient measurements within the backbone show that the image and video objectives quickly become nearly orthogonal, supporting the efficacy of joint optimization without explicit gradient surgery and yielding strong identity fidelity, motion quality, and text alignment compared to both per-subject-tuned and zero-shot SDV-Gen baselines.

Ethics Statement. This work is purely a research project. Currently, we have no plans to incorporate the developed method into a product or expand access to the public. Our research paper accounts for the ethical concerns associated with video generation research. To mitigate issues associated with training data, we have implemented a rigorous filtering process to remove inappropriate content, such as explicit imagery and offensive language, from our training data, thereby minimizing the likelihood of generating inappropriate content.

References

- [1] Yuval Atzmon, Rinon Gal, Yoad Tewel, Yoni Kasten, and Gal Chechik. Multi-shot character consistency for text-to-video generation. *arXiv:2412.07750*, 2024. 2
- [2] Omri Avrahami, Amir Hertz, Yael Vinker, Moab Arar, Shlomi Fruchter, Ohad Fried, Daniel Cohen-Or, and Dani Lischinski. The chosen one: Consistent characters in text-to-image diffusion models. *arXiv:2311.10093*, 2023. 7
- [3] Omer Bar-Tal, Hila Chefer, Omer Tov, Charles Herrmann, Roni Paiss, Shiran Zada, Ariel Ephrat, Junhua Hur, Guanghui Liu, Amit Raj, et al. Lumiere: A space-time diffusion model for video generation. *arXiv preprint arXiv:2401.12945*, 2024. 2
- [4] Andreas Blattmann, Tim Dockhorn, Sumith Kulal, Daniel Mendelevitch, Maciej Kilian, Dominik Lorenz, Yam Levi, Zion English, Vikram Voleti, Adam Letts, et al. Stable video diffusion: Scaling latent video diffusion models to large datasets. *arXiv:2311.15127*, 2023. 1
- [5] Kelvin C.K. Chan, Yang Zhao, Xuhui Jia, Ming-Hsuan Yang, and Huisheng Wang. Improving subject-driven image synthesis with subject-agnostic guidance. In *CVPR*, 2024. 3
- [6] Arslan Chaudhry, Marc’Aurelio Ranzato, Marcus Rohrbach, and Mohamed Elhoseiny. Efficient lifelong learning with a gem. In *International Conference on Learning Representations*, 2019. 3
- [7] Hila Chefer, Shiran Zada, Roni Paiss, Ariel Ephrat, Omer Tov, Michael Rubinstein, Lior Wolf, Tali Dekel, Tomer Michaeli, and Inbar Mosseri. Still-moving: Customized video generation without customized video data. *arXiv:2407.08674*, 2024. 2, 3, 7, 8, 22
- [8] Haoxin Chen, Yong Zhang, Xiaodong Cun, Menghan Xia, Xintao Wang, Chao Weng, and Ying Shan. Videocrafter2: Overcoming data limitations for high-quality video diffusion models, 2024. 2
- [9] Hong Chen, Yipeng Zhang, Simin Wu, Xin Wang, Xuguang Duan, Yuwei Zhou, and Wenwu Zhu. Disenbooth: Identity-preserving disentangled tuning for subject-driven text-to-image generation. In *ICLR*, 2024. 3
- [10] Junsong Chen, Jincheng Yu, Chongjian Ge, Lewei Yao, Enze Xie, Yue Wu, Zhongdao Wang, James Kwok, Ping Luo, Huchuan Lu, and Zhenguo Li. Pixart- α : Fast training of diffusion transformer for photorealistic text-to-image synthesis. *arXiv:2310.00426*, 2023. 3
- [11] Tsai-Shien Chen, Aliaksandr Siarohin, Willi Menapace, Yuwei Fang, Kwot Sin Lee, Ivan Skorokhodov, Kfir Aberman, Jun-Yan Zhu, Ming-Hsuan Yang, and Sergey Tulyakov. Multi-subject open-set personalization in video generation. *arXiv:2501.06187*, 2025. 2, 3
- [12] Zhuowei Chen, Bingchuan Li, Tianxiang Ma, Lijie Liu, Mingcong Liu, Yi Zhang, Gen Li, Xinghui Li, Siyu Zhou, Qian He, and Xinglong Wu. Phantom-data: Towards a general subject-consistent video generation dataset. *arXiv preprint arXiv:2506.18851*, 2025. 3
- [13] Ganggui Ding et al. Freecustom: Tuning-free customized image generation for multi-concept composition. *arXiv:2405.13870*, 2024. 3
- [14] Patrick Esser, Sumith Kulal, Andreas Blattmann, Rahim Entezari, Jonas Müller, Harry Saini, Yam Levi, Dominik Lorenz, Axel Sauer, Frederic Boesel, et al. Scaling rectified flow transformers for high-resolution image synthesis. In *ICML*, 2024. 3
- [15] Robert M French. Catastrophic forgetting in connectionist networks. *Trends in cognitive sciences*, 3(4):128–135, 1999. 3
- [16] Rinon Gal, Yuval Alaluf, Yuval Atzmon, Or Patashnik, Amit H. Bermano, Gal Chechik, and Daniel Cohen-Or. An image is worth one word: Personalizing text-to-image generation using textual inversion. *arXiv preprint arXiv:2208.01618*, 2022. 3
- [17] Yoav HaCohen, Nisan Chiprut, Benny Brazowski, Daniel Shalem, Dudu Moshe, Eitan Richardson, Eran Levin, Guy Shiran, Nir Zabari, Ori Gordon, Poriya Panet, Sapir Weissbuch, Victor Kulikov, Yaki Bitterman, Zeev Melumian, and Ofir Bibi. Ltx-video: Realtime video latent diffusion. *arXiv preprint arXiv:2501.00103*, 2024. 2
- [18] Xuanhua He, Quande Liu, Shengju Qian, Xin Wang, Tao Hu, Ke Cao, Keyu Yan, and Jie Zhang. Id-animator: Zero-shot identity-preserving human video generation. *arXiv:2404.15275*, 2024. 3
- [19] Yingqing He, Tianyu Yang, Yong Zhang, Ying Shan, and Qifeng Chen. Latent video diffusion models for high-fidelity long video generation. 2022. 2
- [20] Wenyi Hong, Ming Ding, Wendi Zheng, Xinghan Liu, and Jie Tang. Cogvideo: Large-scale pretraining for text-to-video generation via transformers. *arXiv:2205.15868*, 2022. 1
- [21] Edward J Hu, Yelong Shen, Phillip Wallis, Zeyuan Allen-Zhu, Yuanzhi Li, Shean Wang, Lu Wang, Weizhu Chen, et al. Lora: Low-rank adaptation of large language models. In *ICLR*, 2022. 4
- [22] Teng Hu, Zhentao Yu, Zhengguang Zhou, Sen Liang, Yuan Zhou, Qin Lin, and Qinglin Lu. Hunyuancustom: A multimodal-driven architecture for customized video generation, 2025. 2, 3
- [23] Zhihao Hu and Dong Xu. Videocontrolnet: A motion-guided video-to-video translation framework by using diffusion model with controlnet. *arXiv:2307.14073*, 2023. 2
- [24] Yuzhou Huang, Ziyang Yuan, Quande Liu, Qiulin Wang, Xintao Wang, Ruimao Zhang, Pengfei Wan, Di Zhang, and Kun Gai. Concept-master: Multi-concept video customization on diffusion transformer models without test-time tuning. *arXiv:2501.04698*, 2025. 2, 3
- [25] Ziqi Huang, Yinan He, Jiashuo Yu, Fan Zhang, Chenyang Si, Yuming Jiang, Yuanhan Zhang, Tianxing Wu, Qingyang Jin,

- Nattapol Chanpaisit, Yaohui Wang, Xinyuan Chen, Limin Wang, Dahua Lin, Yu Qiao, and Ziwei Liu. VBench: Comprehensive benchmark suite for video generative models. In *CVPR*, 2024. 7
- [26] Yuming Jiang, Tianxing Wu, Shuai Yang, Chenyang Si, Dahua Lin, Yu Qiao, Chen Change Loy, and Ziwei Liu. Videobooth: Diffusion-based video generation with image prompts. In *CVPR*, 2024. 2, 3, 6
- [27] Zeyinzi Jiang, Zhen Han, Chaojie Mao, Jingfeng Zhang, Yulin Pan, and Yu Liu. Vace: All-in-one video creation and editing. *arXiv:2503.07598*, 2025. 2, 3, 6, 21, 24, 25
- [28] Wonjoon Jin, Qi Dai, Chong Luo, Seung-Hwan Baek, and Sunghyun Cho. Flovd: Optical flow meets video diffusion model for enhanced camera-controlled video synthesis. *arXiv:2502.08244*, 2025. 19, 20
- [29] jovianzm. Pexels-400k. <https://huggingface.co/datasets/jovianzm/Pexels-400k>, 2025. Accessed: 2025-03-07. 2, 3, 5, 18, 20
- [30] Nupur Kumari, Bingliang Zhang, Richard Zhang, Eli Shechtman, and Jun-Yan Zhu. Multi-concept customization of text-to-image diffusion. In *CVPR*, 2023. 3
- [31] Dongxu Li, Junnan Li, and Steven Hoi. Blip-diffusion: Pre-trained subject representation for controllable text-to-image generation and editing. In *NeurIPS*, 2023. 2, 6
- [32] Jiahe Liu, Youran Qu, Qi Yan, Xiaohui Zeng, Lele Wang, and Renjie Liao. Fréchet video motion distance: A metric for evaluating motion consistency in videos. *arXiv:2407.16124*, 2024. 20
- [33] Lijie Liu, Tianxaing Ma, Bingchuan Li, Zhuowei Chen, Jiawei Liu, Qian He, and Xinglong Wu. Phantom: Subject-consistent video generation via cross-modal alignment. *arXiv:2502.11079*, 2025. 2, 3, 6, 21, 24, 25
- [34] Zhiheng Liu, Yifei Zhang, Yujun Shen, Kecheng Zheng, Kai Zhu, Ruili Feng, Yu Liu, Deli Zhao, Jingren Zhou, and Yang Cao. Customizable image synthesis with multiple subjects. In *Advances in neural information processing systems*, 2023. 3
- [35] David Lopez-Paz and Marc’Aurelio Ranzato. Gradient episodic memory for continual learning. In *Advances in neural information processing systems*, pages 6467–6476, 2017. 3
- [36] Volodymyr Mnih, Koray Kavukcuoglu, David Silver, Andrei A Rusu, Joel Veness, Marc G Bellemare, Alex Graves, Martin Riedmiller, Andreas K Fiedjeland, Georg Ostrovski, et al. Human-level control through deep reinforcement learning. *Nature*, 518(7540):529–533, 2015. 3
- [37] Chong Mou, Xintao Wang, Liangbin Xie, Yanze Wu, Jian Zhang, Zhongang Qi, Ying Shan, and Xiaohu Qie. T2i-adapter: Learning adapters to dig out more controllable ability for text-to-image diffusion models. In *CVPR*, 2023. 3
- [38] William Peebles and Saining Xie. Scalable diffusion models with transformers. In *ICCV*, 2023. 3
- [39] Anthony Robins. Catastrophic forgetting, rehearsal and pseudorehearsal. *Connection Science*, 7(2):123–146, 1995. 3
- [40] Robin Rombach, Andreas Blattmann, Dominik Lorenz, Patrick Esser, and Björn Ommer. High-resolution image synthesis with latent diffusion models. *arXiv:2112.10752*, 2021. 2, 3, 6
- [41] Nataniel Ruiz, Yuanzhen Li, Varun Jampani, Yael Pritch, Michael Rubinstein, and Kfir Aberman. Dreambooth: Fine-tuning text-to-image diffusion models for subject-driven generation. In *CVPR*, 2023. 2, 3, 7
- [42] Hanul Shin, Jung Kwon Lee, Jaehong Kim, and Jiwon Kim. Continual learning with deep generative replay. *Advances in neural information processing systems*, 30, 2017. 3
- [43] Jianlin Su, Yu Lu, Shengfeng Pan, Ahmed Murtadha, Bo Wen, and Yunfeng Liu. Roformer: Enhanced transformer with rotary position embedding. *arXiv:2104.09864*, 2021. 3
- [44] Zhenxiong Tan, Songhua Liu, Xingyi Yang, Qiaochu Xue, and Xinchao Wang. Ominicontrol: Minimal and universal control for diffusion transformer. *arXiv:2411.15098*, 2024. 2, 3, 4, 5, 6, 7, 8, 17, 21, 22, 23, 24, 25
- [45] Zachary Teed and Jia Deng. Raft: Recurrent all-pairs field transforms for optical flow. *arXiv:2003.12039*, 2020. 20
- [46] Yoad Tewel, Omri Kaduri, Rinon Gal, Yoni Kasten, Lior Wolf, Gal Chechik, and Yuval Atzmon. Training-free consistent text-to-image generation. *TOG*, 2024. 3
- [47] Jianyi Wang, Zhijie Lin, Meng Wei, Yang Zhao, Ceyuan Yang, Chen Change Loy, and Lu Jiang. Seedvr: Seeding infinity in diffusion transformer towards generic video restoration. In *Proceedings of the IEEE/CVF Conference on Computer Vision and Pattern Recognition (CVPR)*, pages 2161–2172, 2025. 2
- [48] Xiaowei Wang, Siming Fu, Qihan Huang, Wanggui He, and Hao Jiang. Ms-diffusion: Multi-subject zero-shot image personalization with layout guidance. *arXiv:2406.07209*, 2024. 3
- [49] WanTeam et al. Wan: Open and advanced large-scale video generative models. *arXiv preprint arXiv:2503.20314*, 2025. 1, 2, 6
- [50] Yujie Wei, Shiwei Zhang, Zhiwu Qing, Hangjie Yuan, Zhiheng Liu, Yu Liu, Yingya Zhang, Jingren Zhou, and Hongming Shan. Dreamvideo: Composing your dream videos with customized subject and motion. In *CVPR*, 2024. 2, 3
- [51] Yujie Wei, Shiwei Zhang, Hangjie Yuan, Xiang Wang, Haonan Qiu, Rui Zhao, Yutong Feng, Feng Liu, Zhizhong Huang, Jiaxin Ye, et al. Dreamvideo-2: Zero-shot subject-driven video customization with precise motion control. *arXiv:2410.13830*, 2024. 2, 3
- [52] Jianzong Wu, Xiangtai Li, Yanhong Zeng, Jiangning Zhang, Qianyu Zhou, Yining Li, Yunhai Tong, and Kai Chen. Motionbooth: Motion-aware customized text-to-video generation. *arXiv:2406.17758*, 2024. 3
- [53] Tao Wu, Yong Zhang, Xintao Wang, Xianpan Zhou, Guangcong Zheng, Zhongang Qi, Ying Shan, and Xi Li. Customcrafter: Customized video generation with preserving motion and concept composition abilities. In *AAAI*, 2025. 2, 3, 7, 8, 21, 23
- [54] Zhuoyi Yang, Jiayan Teng, Wendi Zheng, Ming Ding, Shiyu Huang, Jiazheng Xu, Yuanming Yang, Wenyi Hong, Xiaohan Zhang, Guanyu Feng, et al. Cogvideox: Text-to-video diffusion models with an expert transformer. *arXiv:2408.06072*, 2024. 1, 3, 6, 12, 20

- [55] Hu Ye, Jun Zhang, Sibao Liu, Xiao Han, and Wei Yang. Ip-adapter: Text compatible image prompt adapter for text-to-image diffusion models. *arXiv:2308.06721*, 2023. 2, 3, 6
- [56] Tianhe Yu, Saurabh Kumar, Abhishek Gupta, Sergey Levine, Karol Hausman, and Chelsea Finn. Gradient surgery for multi-task learning. In *Advances in Neural Information Processing Systems*, 2020. 3, 6, 8
- [57] Shenghai Yuan, Jinfa Huang, Xianyi He, Yunyuan Ge, Yujun Shi, Liuhan Chen, Jiebo Luo, and Li Yuan. Identity-preserving text-to-video generation by frequency decomposition. *arXiv:2411.17440*, 2024. 2, 3
- [58] Shenghai Yuan, Xianyi He, Yufan Deng, Yang Ye, Jinfa Huang, Bin Lin, Jiebo Luo, and Li Yuan. Opens2v-nexus: A detailed benchmark and million-scale dataset for subject-to-video generation. *arXiv preprint arXiv:2505.20292*, 2025. 3, 20, 21
- [59] Yu Zeng, Vishal M. Patel, Haochen Wang, Xun Huang, Ting-Chun Wang, Ming-Yu Liu, and Yogesh Balaji. Jedi: Joint-image diffusion models for finetuning-free personalized text-to-image generation. In *CVPR*, 2024. 3
- [60] Lvmin Zhang, Anyi Rao, and Maneesh Agrawala. Adding conditional control to text-to-image diffusion models. In *ICCV*, 2023. 3
- [61] Yuxuan Zhang, Yiren Song, Jiaming Liu, Rui Wang, Jinpeng Yu, Hao Tang, Huaxia Li, Xu Tang, Yao Hu, Han Pan, et al. Ssr-encoder: Encoding selective subject representation for subject-driven generation. In *CVPR*, 2024. 3
- [62] Yuechen Zhang, Yaoyang Liu, Bin Xia, Bohao Peng, Zexin Yan, Eric Lo, and Jiaya Jia. Magic mirror: Id-preserved video generation in video diffusion transformers. In *ICCV*, 2025. 2, 3

Subject-driven Video Generation via Disentangled Identity and Motion

Supplementary Material

Note: We use **green** color to refer to figures, tables in the main manuscript (e.g., Figure 2) and use **blue** color to refer to figures, tables in this supplementary material (e.g., Figure 1).

Algorithm 1: Dual-task Learning for Subject-Driven Video Generation

```
Input : Pretrained CogVideoX-5b  $f_\theta$  with LoRA adapters;
         Image dataset  $\mathcal{D}_{\text{img}}$  (paired left/right views with metadata);
         Proxy video dataset  $\mathcal{D}_{\text{vid}}$  (text–video pairs with cached latents and ref frames);
         Replay probability  $p=0.2$ ;
         RandomFrameSelect(),
TokenDrop( $p_{\text{drop}}=0.5$ ), on-the-fly decode/crop.
Output: Fine-tuned  $f_\theta$  balancing identity fidelity and motion coherence

Problem Decomposition:
• Identity learning: inject subject features from  $\mathcal{D}_{\text{img}}$  with random crop/jitter and view drop
• motion-awareness preservation: maintain motion priors via proxy replay from  $\mathcal{D}_{\text{vid}}$ 

foreach iteration  $t \leftarrow 1, \dots, T_{\text{max}}$  do
  Sample  $u \sim \mathcal{U}(0, 1)$  for stochastic task selection
  if  $u < p$  then
    /* Motion-awareness preservation:
       video path */
    Decode batch  $\{(T_i, V_i)\}$  from  $\mathcal{D}_{\text{vid}}$  to  $720 \times 480$ ,
    8 fps (max 49 frames)
     $\mathbf{f}_{\text{ref}} \leftarrow \text{RandomFrameSelect}(V_i)$ 
    // mitigate frame bias
     $\mathbf{X}_{\text{ref}} \leftarrow \text{TokenDrop}(\text{VAE}(\mathbf{f}_{\text{ref}}), p_{\text{drop}})$ 
    // drop ref tokens
    Compute  $\mathcal{L}_{\text{vid}}(T_i, V_i, \mathbf{X}_{\text{ref}})$  via v-prediction
     $\mathbf{g}_{\text{vid}} \leftarrow \nabla_{\theta} \mathcal{L}_{\text{vid}}; \theta \leftarrow \theta - \eta \mathbf{g}_{\text{vid}}$ 
  else
    /* Identity learning: image path
       */
    Decode paired views  $\{(I_i^{\text{src}}, I_i^{\text{tgt}})\}$  from  $\mathcal{D}_{\text{img}}$  with
    crop jitter and optional view drop
    Apply LoRA-only updates on subject-token
    pathways
    Compute  $\mathcal{L}_{\text{img}}(I_i^{\text{src}}, I_i^{\text{tgt}})$  via v-prediction
     $\mathbf{g}_{\text{img}} \leftarrow \nabla_{\theta} \mathcal{L}_{\text{img}}; \theta \leftarrow \theta - \eta \mathbf{g}_{\text{img}}$ 
  /* Optional: monitor gradient
    interactions (off by default) */
  if  $t \bmod 100 = 0$  then
     $\phi_t \leftarrow \cos(\mathbf{g}_{\text{img}}, \mathbf{g}_{\text{vid}})$  // conflict
    tracking / orthogonality

return  $f_\theta$ 
```

In this section, we provide additional details on our zero-shot subject-driven video (SDV-Gen) framework, including full pseudocode for the proposed method and extended ablation results that further validate our design choices.

A. Implementation Details

Our subject-driven video generation (SDV-Gen) framework, as outlined in Algorithm 1, begins by initializing a pre-trained multi-modal diffusion transformer f_θ (e.g., CogVideoX [54]), which already possesses general text–visual alignment and motion priors. Two datasets are made available: the first is an paired subject-image set \mathcal{D}_{img} containing image pairs $(I^{(1)}, I^{(2)})$ depicting the same subject under varying poses or contexts, and the second is an unpaired video set \mathcal{D}_{vid} consisting of text-video pairs (T, V) . Our key insight is to *factorize* SDV-Gen into two tasks: Identity injection and motion-awareness preservation and then interleave them stochastically during training.

At each training iteration, a uniform random variable u is drawn from $\mathcal{U}(0, 1)$. If $u < p$, we sample a mini-batch of unpaired videos (T_i, V_i) and perform a *motion-aware phase* (I2V fine-tuning). This phase leverages the random frame selection and image-token dropping steps (RandomFrameSelect and TokenDrop) to discourage the model from fixating on a single reference frame. By computing the video reconstruction loss $\mathcal{L}_{\text{vid}}(T_i, V_i)$, we update f_θ to maintain or recover realistic motion characteristics. Alternatively, if $u \geq p$, we focus on an *identity phase*, sampling a mini-batch of paired subject-images $(I_i^{(1)}, I_i^{(2)})$ from \mathcal{D}_{img} and minimizing the identity injection loss $\mathcal{L}_{\text{img}}(I_i^{(1)}, I_i^{(2)})$. Crucially, we only tune the LoRA-based parameters associated with the subject-specific pathways \mathbf{X}_{in} , preserving the model’s capacity to handle text tokens \mathbf{C}_T and output frames \mathbf{X}_{out} .

A.1. LoRA Configuration

We insert rank-128 LoRA adapters with scaling $\alpha=64$ into the transformer. Adapters are attached to the attention projections (to_q, to_k, to_v, to_out.0) and selected MLP/normalization-associated projections (e.g., proj, text_proj, norm1.linear, norm2.linear, ff.net.2). Base weights remain frozen, only LoRA parameters receive gradients. Normalization layers themselves (scale/bias) are not updated directly, any normalization-related adaptation occurs solely via the attached LoRA modules. We denote the union of all trainable parameters by θ_{train} , which is also the set used for gradient logging in Sec. B. Gradient checkpointing is enabled for memory efficiency.

A.2. Full Training Setup.

We train in bfloat16 with TF32 enabled, using tiling/slicing to improve memory locality. Sequences comprise up to 49 frames at 720×480 and 8 fps (decode at a higher target fps, then sub-sample to 8 fps for training). Optimization uses AdamW with learning rate 5×10^{-5} , $\beta_1=0.9$, $\beta_2=0.95$, cosine-with-restarts with 200

warmup steps, and gradient clipping at 1.0. We train for 30 epochs with a global batch size of 32, saving checkpoints every 50 steps. The identity stream applies per-view random-crop jitter and occasionally drops one reference view with probability 0.5 to mitigate pose overfitting.

By stochastically switching between these two objectives with mixing probability p (we use $p=0.2$), the model balances subject fidelity and temporal consistency throughout training, avoiding the pitfalls of purely sequential or single-focus approaches. After T_{\max} iterations, f_{θ} emerges as a zero-shot SDV-Gen model capable of generating videos that simultaneously preserve the subject’s identity and exhibit coherent motion, even though no large-scale annotated SDV-Gen dataset is required.

B. Gradient Measurement and Analysis

B.1. Measurement Protocol

Measuring full gradients of a multi-billion-parameter model is memory-intensive. We therefore follow multi-task learning practice and compute on the LoRA parameters actually updated during fine-tuning, denoted θ_{train} .

Trained Parameters. We compute statistics over the same trainable set θ_{train} defined in Sec. A (LoRA adapters on attention and selected projection layers; base weights and normalization scale/bias remain frozen).

At a checkpoint θ_t , we freeze parameters and assemble two validation mini-batches, using the same preprocessing as training unless noted:

- **Paired subject-images:** $(I^{(1)}, I^{(2)}, P)$ sampled from the validation split, disjoint from training subjects. Images are decoded to 720×480 with the same preprocessing as training (random crop jitter enabled; no view drop during measurement). Prompts P are tokenized exactly as in training.
- **Unpaired videos:** (T, V) sampled from the validation split of the unpaired video corpus. Videos are decoded on-the-fly, resized to 720×480 , and truncated to at most 49 frames rendered at 8 or 16 fps. A reference frame is selected uniformly at random (RandomFrameSelect).

Timestep Sampling and Objective. We use the same diffusion scheduler as in Sec. A. For each sample, draw a timestep $\tau \sim \text{Unif}\{0, \dots, N-1\}$ and add Gaussian noise according to the scheduler; the target is formed via velocity parameterization. We then compute gradients with respect to θ_{train} :

$$\begin{aligned} g_{\text{img}}(t) &= \nabla_{\theta_{\text{train}}} \mathcal{L}_{\text{img}}(I^{(1)}, I^{(2)}, P), \\ g_{\text{vid}}(t) &= \nabla_{\theta_{\text{train}}} \mathcal{L}_{\text{vid}}(T, V). \end{aligned}$$

DDP Pre-sync Capture and Aggregation. In distributed data parallel training, we record *pre-allreduce* gradients to avoid distortion from cross-rank synchronization. For each dataset (Paired subject-images/Unpaired videos) and before any optimizer step:

1. Register backward hooks on modules containing θ_{train} to copy per-parameter `.grad` into a preallocated flat buffer in a fixed parameter order.

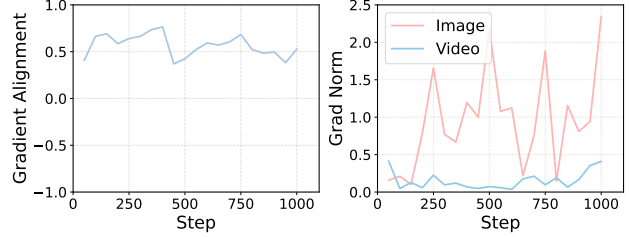


Figure 9. **Gradient alignment between image and video batches during image-only finetuning and gradient norms of two objectives.** Recorded gradient alignment and norm every 50 steps.

2. Capture the flat gradient on each rank before the framework performs all-reduce.
3. Reconstruct the global gradient by reducing the sum of the flat buffers across ranks and dividing by the world size (equivalent to an average pre-sync gradient at the current step).
4. Move the aggregated flat gradient to the CPU for logging to minimize device memory pressure. When gradient accumulation is used, we first accumulate local micro-batches, then capture the pre-sync aggregate.

Flattening and Layer-wise Grouping. Let $\tilde{g}_{\text{img}}(t)$ and $\tilde{g}_{\text{vid}}(t)$ be the aggregated flat vectors formed by concatenating per-parameter gradients from θ_{train} in a deterministic module/parameter order, skipping None entries. We also maintain indices to recover layer-wise blocks (e.g., attention vs. MLP-associated projections) for per-group statistics.

Cosine Similarity and Norms. We report the cosine similarity and L2 norms:

$$\phi(t) = \frac{\langle \tilde{g}_{\text{img}}(t), \tilde{g}_{\text{vid}}(t) \rangle}{\|\tilde{g}_{\text{img}}(t)\|_2 \|\tilde{g}_{\text{vid}}(t)\|_2 + \varepsilon},$$

with a small ε to avoid division by zero. When desired, we compute the same statistics per layer group by slicing the flat vectors using the stored indices.

Cadence and Compared Strategies. We repeat the above every K training steps (we use $K=5$ to 50 depending on the experiment.), holding the evaluation seed fixed and reusing the same validation batches over time for comparability. We compare: (a) SDI-Gen-only fine-tuning ($p=0$), (b) our stochastic dual-task learning ($p=0.2$).

B.2. Image-only Finetuning and Comparison

We now probe the gradient behaviour of a pure SDI-Gen set fine-tuning regime ($p=0$), where all optimizer steps are taken on \mathcal{L}_{img} and the video loss \mathcal{L}_{vid} is never used for training. At checkpoints between steps 50 and 1000, we freeze θ and measure $g_{\text{img}}(t)$ and $g_{\text{vid}}(t)$ on fixed held-out image and video mini-batches following the protocol in Sec. B; the resulting norms and cosine similarities are shown in Fig. 9.

Norms vs. the Dual-task Schedule. In the main paper, Fig. 5 shows that under our stochastic dual-task schedule the norms of $g_{\text{img}}(t)$ and $g_{\text{vid}}(t)$ rapidly settle to a similar and relatively small scale after the first ~ 100 steps and remain non-negligible but stable thereafter. In contrast, the image-only run in Fig. 9 exhibits persistently large and highly fluctuating image gradients: $\|g_{\text{img}}(t)\|_2$ grows well beyond the range observed in Fig. 5 and does not decay to a steady plateau. At the same time, the video gradient norm stays clearly non-zero and is substantially larger than in the dual-task case, even though \mathcal{L}_{vid} is never optimized. This indicates that image gradient updates continue to inject strong gradients into the shared LoRA subspace along directions that the video objective remains sensitive to, rather than gradually stabilizing that subspace, as in the dual-task setting.

Alignment vs. Emergent Orthogonality. Figure 5 in the main paper shows that, under dual-task training, the cosine similarity $\phi(t) = \cos \angle(g_{\text{img}}(t), g_{\text{vid}}(t))$ rapidly collapses into a narrow band around zero and stays there, revealing an emergent near-orthogonality between identity and temporal gradients while their norms remain non-vanishing. By contrast, in the image-only run, the cosine in Fig. 9 never approaches this orthogonal regime; after an initial transient, it stays strongly positive, typically in the 0.4–0.75 range across checkpoints. Pure image fine-tuning thus does not lead to the decoupling observed in Fig. 5 and instead keeps g_{img} and g_{vid} acting through highly overlapping directions in the LoRA parameter subspace.

Implications for Temporal Behavior. At first glance, a large positive cosine might seem desirable, since it suggests that the two gradients would cooperate if both were optimized simultaneously. In the image-only setting, however, the optimizer follows only $-g_{\text{img}}(t)$. The strong and persistent alignment in Fig. 9, combined with the large and highly variable gradient norms, implies that each identity step makes a substantial update in directions to which the video loss is also sensitive, yet no video gradient is applied to regularize or correct this drift. Empirically, this matches the behavior of the “Image-only” baseline in Tab. 3 of the main manuscript, which achieves high motion smoothness but almost zero dynamic degree, indicating near zero-motion (“frozen”) videos despite strong identity scores. Comparing Fig. 5 with Fig. 9 thus suggests that our stochastic dual-task schedule is crucial for decoupling identity and temporal directions in parameter space, allowing identity injection to proceed without continuously eroding the pretrained motion prior.

B.3. PCGrad Details and Comparison

PCGrad in Our Dual-task Setting. We consider the two objectives used in the main paper (identity injection and motion-awareness preservation) and apply Projected Conflicting Gradient (PCGrad) at the level of task gradients computed on the trainable set θ_{train} (Sec. A). At a given iteration we first obtain pre-synchronization gradients g_{img} and g_{vid} as in Sec. B. PCGrad then

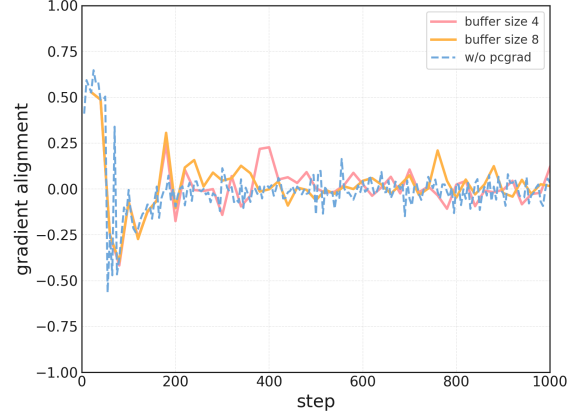


Figure 10. **Gradient alignment comparison of the two objectives when applying PCGrad or not.** Red and Orange line indicate the alignment result with PCGrad with different buffer sizes, and blue dashed line indicates the alignment without PCGrad, equivalent to Fig. 5 in the main manuscript.

removes components responsible for pairwise conflicts:

$$\tilde{g}_{\text{img}} = g_{\text{img}} - \mathbf{1}[\langle g_{\text{img}}, g_{\text{vid}} \rangle < 0] \frac{\langle g_{\text{img}}, g_{\text{vid}} \rangle}{\|g_{\text{vid}}\|_2^2 + \varepsilon} g_{\text{vid}},$$

$$\tilde{g}_{\text{vid}} = g_{\text{vid}} - \mathbf{1}[\langle g_{\text{vid}}, g_{\text{img}} \rangle < 0] \frac{\langle g_{\text{vid}}, g_{\text{img}} \rangle}{\|g_{\text{img}}\|_2^2 + \varepsilon} g_{\text{img}},$$

where ε stabilizes divisions for small norms. The final update direction is $g^* = (1-p)g_{\text{img}} + p\tilde{g}_{\text{vid}}$ with changing probability of p . In practice, we implement PCGrad in a *buffered* fashion: as training proceeds, we maintain a short FIFO buffer of recent pre-sync gradients annotated by domain and apply the projection once both domains have appeared within the buffer. This avoids doubling the per-iteration cost and lets us trade off temporal smoothing of gradients against recency by changing the buffer size.

Gradient Alignment under PCGrad. Figure 10 reports the cosine similarity between g_{img} and g_{vid} when PCGrad is used during training with two buffer sizes (4 and 8). Both variants quickly push the gradient cosine into a narrow band around zero and keep it there, with only small differences between buffer sizes. The resulting curves are very close to those obtained with our default stochastic dual-task schedule in blue dashed line in Fig. 10 (Equivalent to that of Fig. 5 in the main manuscript), indicating that stochastic interleaving plus proxy replay already induces near-orthogonality between image and video-batch gradients. In particular, increasing the buffer length from 4 to 8 yields only minor changes in the alignment trajectory, suggesting that most of the benefit comes from the dual-task geometry itself rather than from explicit projections over a longer history.

Why We Keep the Simpler Schedule. Although PCGrad slightly accelerates the convergence in early iterations, we observe only marginal differences in downstream metrics and qualitative samples compared to our default method. This is consistent with the observation that (i) the stochastic task-switching with mixing probability p already reduces gradient conflict, (ii) updates are

Table 5. Quantitative comparison on applying PCGrad.

Training Method	Motion Smoothness	Dynamic Degree	CLIP-T	CLIP-I	DINO-I
w/ PCGrad + buffer 8	98.86	50.83	31.28	82.17	74.32
w/ PCGrad + buffer 4	97.74	70.83	33.44	74.52	56.15
w/o PCGrad	98.45	69.64	32.69	77.14	62.88

confined to low-rank LoRA adapters where the representational overlap between tasks is limited, and (iii) the replay ratio biases most steps toward image gradient updates, so genuine conflicts are relatively rare. Given this, the additional complexity of maintaining gradient buffers and performing projections offers limited practical gains in our setting. We therefore adopt the stochastic dual-task schedule without PCGrad as our main training recipe and regard PCGrad as an optional refinement that produces similar gradient-alignment behavior, as illustrated in Fig. 10.

Quantitative Comparison on VBench. We evaluate default stochastic dual-task training (without PCGrad) and its PCGrad-augmented counterpart on VBench. We report text alignment, subject consistency, motion smoothness, and overall quality metrics using the same evaluation protocol and sampling setup as in Sec. A. Across settings, we observe that headline VBench scores are similar between the two, with differences within experimental variance; see Table 5 for full results.

C. Theoretical Analysis

In this section, we provide a stylized analysis that complements Proposition 4.1 in the main paper and the empirical gradient measurements in Figs. 5 and Figs. 9–10. We work with a local second-order model for both objectives and show that, under dual-task learning, the gradient inner product decays to zero. In contrast, under image-only fine-tuning, it typically converges to a non-zero constant. We then use the same framework to explain why PCGrad yields only marginal gains once gradients are already nearly orthogonal. Throughout this section, the analysis is intended purely as intuition for the observed gradient dynamics, not as a rigorous description of large diffusion transformers.

C.1. Setup and Notation

Let $L_1 : \mathbb{R}^n \rightarrow \mathbb{R}$ (identity loss) and $L_2 : \mathbb{R}^n \rightarrow \mathbb{R}$ (temporal loss) be two objectives with gradients

$$g_1(\theta) = \nabla_{\theta} L_1(\theta), \quad g_2(\theta) = \nabla_{\theta} L_2(\theta).$$

Gradient Conflict. We measure the interaction between the two tasks by the cosine of the angle between their gradients:

$$\phi(\theta) = \cos \angle(g_1(\theta), g_2(\theta)) = \frac{\langle g_1(\theta), g_2(\theta) \rangle}{\|g_1(\theta)\| \|g_2(\theta)\|}. \quad (6)$$

Stochastic Task Switching. The training rule in the main paper alternates between updates on L_1 and L_2 :

$$\theta_{t+1} = \theta_t - \eta g_t, \quad g_t = \begin{cases} g_1(\theta_t), & \text{w.p. } 1-p, \\ g_2(\theta_t), & \text{w.p. } p, \end{cases} \quad (7)$$

so that the expected update direction equals the gradient of the mixture loss

$$\bar{L}(\theta) = (1-p)L_1(\theta) + pL_2(\theta), \quad \mathbb{E}[g_t | \theta_t] = \nabla_{\theta} \bar{L}(\theta_t). \quad (8)$$

The dual-task schedule in Sec. 4 of the main paper can therefore be viewed as stochastic gradient descent on \bar{L} , with L_1 and L_2 sampled according to the mixing probability p .

C.2. Local Second-Order Mixture Model

We focus on the behavior in a neighborhood of a point θ^* where both tasks are approximately stationary.

Assumption C.2.1 (Local second-order behavior). *There exists a point θ^* and symmetric matrices $H_1, H_2 \in \mathbb{R}^{n \times n}$ such that, in a neighborhood of θ^* , the losses are twice differentiable with Hessians $H_i(\theta^*)$ and*

$$L_i(\theta) \approx L_i(\theta^*) + \frac{1}{2}(\theta - \theta^*)^{\top} H_i(\theta - \theta^*), \quad i \in \{1, 2\}, \quad (9)$$

so that the corresponding gradients satisfy the local linearization

$$g_i(\theta) \approx H_i(\theta - \theta^*), \quad i \in \{1, 2\}. \quad (10)$$

We assume H_1 and H_2 are positive semi-definite and approximately commute, i.e., they are (up to a small perturbation) simultaneously diagonalizable in this local region.

This second-order approximation is standard around critical points. Commutativity means that near θ^* the two tasks share a common set of principal directions, which lets us express the dynamics in a joint eigenbasis.

Assumption C.2.2 (Positive curvature of the mixture along the trajectory). *Let*

$$M := (1-p)H_1 + pH_2. \quad (11)$$

We assume that, restricted to the subspace explored by training (the span of $\theta_0 - \theta^*$), M is positive definite, i.e., all eigenvalues μ_k of M on this subspace satisfy

$$0 < \mu_{\min} \leq \mu_k \leq \mu_{\max} < \infty. \quad (12)$$

Note that Assumption C.2.2 only requires positive curvature for the mixture \bar{L} along the trajectory we care about, rather than global strong convexity of each task.

C.3. Dual-Task Learning and Gradient Interaction

Under Assumptions C.2.1–C.2.2, we can make the statement of Proposition 4.1 concrete in this local model.

Proposition C.3.1 (Local model behind Proposition 4.1). *Assume the local second-order model (Assumption C.2.1) and the positive-curvature condition on the mixture (Assumption C.2.2). Consider deterministic gradient descent on \bar{L} with step size $0 < \eta < 1/\mu_{\max}$,*

$$\theta_{t+1} = \theta_t - \eta \nabla \bar{L}(\theta_t) = \theta_t - \eta [(1-p)g_1(\theta_t) + pg_2(\theta_t)]. \quad (13)$$

In this local model, the gradients evolve linearly, and the inner product

$$A_t \equiv \langle g_1(\theta_t), g_2(\theta_t) \rangle$$

decays exponentially:

$$|A_t| \leq C(1 - \eta\mu_{\min})^{2t}, \quad \text{for some constant } C > 0, \quad (14)$$

and in particular $\lim_{t \rightarrow \infty} A_t = 0$.

Proof. Let $z_t := \theta_t - \theta^*$. Under the local linearization,

$$g_1(\theta_t) \approx H_1 z_t, \quad g_2(\theta_t) \approx H_2 z_t,$$

and the gradient of the mixture loss is

$$\nabla \bar{L}(\theta_t) \approx (1-p)H_1 z_t + p H_2 z_t = M z_t.$$

The gradient descent update (13) therefore becomes

$$z_{t+1} = \theta_{t+1} - \theta^* \approx \theta_t - \theta^* - \eta M z_t = (I - \eta M) z_t.$$

By Assumption C.2.1, H_1 and H_2 commute and hence are simultaneously diagonalizable with M (ignoring the small perturbation in this toy model). Let U be the orthonormal matrix of shared eigenvectors and write

$$H_1 = U \Lambda_1 U^\top, \quad H_2 = U \Lambda_2 U^\top, \quad M = U M U^\top,$$

where $\Lambda_1 = \text{diag}(\lambda_k^{(1)})$, $\Lambda_2 = \text{diag}(\lambda_k^{(2)})$ and $M = \text{diag}(\mu_k)$. In these coordinates $z_t = U c_t$ for some coefficients $c_t \in \mathbb{R}^n$ and the update simplifies to

$$c_{t+1} = (I - \eta M) c_t, \quad c_t = (I - \eta M)^t c_0,$$

so that each component evolves as

$$c_{t,k} = (1 - \eta \mu_k)^t c_{0,k}.$$

The gradients in this basis are

$$g_1(\theta_t) \approx U \Lambda_1 c_t, \quad g_2(\theta_t) \approx U \Lambda_2 c_t,$$

and their inner product is

$$\begin{aligned} A_t &\approx \langle g_1(\theta_t), g_2(\theta_t) \rangle = c_t^\top \Lambda_1 \Lambda_2 c_t \\ &= \sum_k \lambda_k^{(1)} \lambda_k^{(2)} c_{t,k}^2 = \sum_k \lambda_k^{(1)} \lambda_k^{(2)} (1 - \eta \mu_k)^{2t} c_{0,k}^2. \end{aligned}$$

Using Assumption C.2.2, $0 < \mu_{\min} \leq \mu_k \leq \mu_{\max}$ on the subspace reached by training, and since $\eta < 1/\mu_{\max}$ we have $0 \leq 1 - \eta \mu_k \leq 1 - \eta \mu_{\min} < 1$. Therefore

$$|A_t| \leq \left(\max_k |\lambda_k^{(1)} \lambda_k^{(2)}| \right) \|c_0\|^2 (1 - \eta \mu_{\min})^{2t} = C(1 - \eta \mu_{\min})^{2t},$$

for some constant $C > 0$ depending only on the initial point and the local Hessians. This proves the exponential decay (14) and hence $\lim_{t \rightarrow \infty} A_t = 0$ in this local model. \square

Connection to Proposition 4.1 and Empirical Trends.

In the main manuscript we measure the cosine similarity between the image and video gradients, $\phi(t) = \cos \angle(g_{\text{img}}(t), g_{\text{vid}}(t))$, and empirically observe that it rapidly converges to a narrow band around zero while the gradient norms remain non-negligible (Figs. 5). Proposition C.3.1 shows that, in a local second-order model where the two tasks share a common eigenbasis and the mixture has positive curvature along the trajectory, gradient descent on the mixture loss naturally drives the inner product $\langle g_1, g_2 \rangle$ (and hence its cosine) toward zero. This toy result should be read as one concrete instance consistent with Proposition 4.1, not as a formal guarantee for deep diffusion transformers.

C.4. Image-Only Fine-Tuning in the Same Model

We now show that in the same framework, pure image-only fine-tuning ($p = 0$) is not expected to drive the cosine toward zero. This matches the behavior observed in Fig. 9, where the cosine remains strongly positive throughout training.

Proposition C.4.1 (Image-only fine-tuning). *Assume the setting of Assumption C.2.1 and suppose that H_1 is positive definite on the subspace explored by training. Consider gradient descent on L_1 alone,*

$$\theta_{t+1} = \theta_t - \eta g_1(\theta_t), \quad 0 < \eta < 2/\lambda_{\max}(H_1), \quad (15)$$

and define $A_t = \langle g_1(\theta_t), g_2(\theta_t) \rangle$ and $\phi(t)$ as in (6). Let k^* be an index of an eigenvalue of H_1 with maximal magnitude on the trajectory, i.e., $|\lambda_{k^*}^{(1)}| = \max_k |\lambda_k^{(1)}|$ and $c_{0,k^*} \neq 0$. Then in the local model,

$$\lim_{t \rightarrow \infty} \phi(t) = \text{sign}(\lambda_{k^*}^{(1)} \lambda_{k^*}^{(2)}), \quad (16)$$

and in particular the cosine converges to a non-zero constant whenever $\lambda_{k^*}^{(1)} \lambda_{k^*}^{(2)} \neq 0$.

Proof. Under the image-only update $z_{t+1} = (I - \eta H_1) z_t$ with $z_t = \theta_t - \theta^*$, the same eigenbasis U as in the previous proof diagonalizes H_1 and H_2 . Writing $z_t = U c_t$ gives $c_{t+1,k} = (1 - \eta \lambda_k^{(1)}) c_{t,k}$ and hence

$$c_{t,k} = (1 - \eta \lambda_k^{(1)})^t c_{0,k}.$$

Because H_1 is positive definite on the relevant subspace and $0 < \eta < 2/\lambda_{\max}(H_1)$, we have $|1 - \eta \lambda_k^{(1)}| < 1$ for all k , and the component with largest $|\lambda_k^{(1)}|$ dominates as $t \rightarrow \infty$. More precisely, for $k \neq k^*$,

$$\frac{c_{t,k}}{c_{t,k^*}} = \left(\frac{1 - \eta \lambda_k^{(1)}}{1 - \eta \lambda_{k^*}^{(1)}} \right)^t \frac{c_{0,k}}{c_{0,k^*}} \rightarrow 0.$$

Thus z_t aligns with v_{k^*} , the k^* th column of U , and the gradients satisfy

$$g_1(\theta_t) \approx \lambda_{k^*}^{(1)} c_{t,k^*} v_{k^*}, \quad g_2(\theta_t) \approx \lambda_{k^*}^{(2)} c_{t,k^*} v_{k^*},$$

up to asymptotically negligible contributions from other modes. Therefore

$$\lim_{t \rightarrow \infty} \phi(t) = \lim_{t \rightarrow \infty} \frac{\langle g_1(\theta_t), g_2(\theta_t) \rangle}{\|g_1(\theta_t)\| \|g_2(\theta_t)\|} = \text{sign}(\lambda_{k^*}^{(1)} \lambda_{k^*}^{(2)}),$$

which is non-zero whenever $\lambda_{k^*}^{(1)} \lambda_{k^*}^{(2)} \neq 0$. \square

This proposition explains why, in Fig. 9, the cosine between image and video gradients remains strongly positive under image-only fine-tuning. In the local model, the optimization path aligns with a dominant eigen-direction of H_1 , and if H_2 has positive curvature along the same direction, then g_1 and g_2 stay positively aligned instead of becoming orthogonal. Because the optimizer follows only $-g_1$ in this regime, every identity update moves parameters along directions to which the video objective is also highly sensitive, without any counter-balancing video gradient, which is consistent with the near-static yet identity-faithful behavior of the image-only baseline in Table 3.

C.5. Effect of PCGrad in the Local Model

We finally use the same framework to explain why PCGrad yields gradient alignment curves similar to our default dual-task schedule (Fig. 10) and only marginal gains in downstream metrics (Table 6).

PCGrad Update for Dual-tasks. For two tasks with gradients g_1 and g_2 , PCGrad projects away conflicting components when $\langle g_1, g_2 \rangle < 0$. In the two-task case, the projected gradients are

$$\tilde{g}_1 = g_1 - \mathbf{1}[\langle g_1, g_2 \rangle < 0] \frac{\langle g_1, g_2 \rangle}{\|g_2\|^2} g_2, \quad (17)$$

$$\tilde{g}_2 = g_2 - \mathbf{1}[\langle g_2, g_1 \rangle < 0] \frac{\langle g_2, g_1 \rangle}{\|g_1\|^2} g_1. \quad (18)$$

Given mixing probability p , the PCGrad update direction is $g^{\text{PC}} = (1-p)\tilde{g}_1 + p\tilde{g}_2$, whereas the dual-task schedule without projection uses the mixture gradient $g^{\text{mix}} = (1-p)g_1 + pg_2$.

Lemma C.5.1 (Difference between PCGrad and mixture update). *Let $A = \langle g_1, g_2 \rangle$ and suppose $A < 0$ so that PCGrad modifies both gradients. Then the difference between the PCGrad and mixture updates satisfies*

$$\|g^{\text{PC}} - g^{\text{mix}}\| \leq |A| \left(\frac{1-p}{\|g_2\|} + \frac{p}{\|g_1\|} \right) \leq 2|A| \max \left\{ \frac{1}{\|g_1\|}, \frac{1}{\|g_2\|} \right\}, \quad (19)$$

and in particular

$$\frac{\|g^{\text{PC}} - g^{\text{mix}}\|}{\|g^{\text{mix}}\|} \leq C_{\text{rel}} |\cos \angle(g_1, g_2)|, \quad (20)$$

for some constant C_{rel} depending only on the ratio of $\|g_1\|$ and $\|g_2\|$.

Proof. When $A < 0$ we have

$$\tilde{g}_1 - g_1 = -\frac{A}{\|g_2\|^2} g_2, \quad \tilde{g}_2 - g_2 = -\frac{A}{\|g_1\|^2} g_1,$$

and therefore

$$g^{\text{PC}} - g^{\text{mix}} = (1-p)(\tilde{g}_1 - g_1) + p(\tilde{g}_2 - g_2) = -A \left(\frac{1-p}{\|g_2\|^2} g_2 + \frac{p}{\|g_1\|^2} g_1 \right).$$

Taking norms gives

$$\|g^{\text{PC}} - g^{\text{mix}}\| \leq |A| \left(\frac{1-p}{\|g_2\|} + \frac{p}{\|g_1\|} \right),$$

and the second inequality in (19) follows by bounding each coefficient by the maximum of $1/\|g_1\|$ and $1/\|g_2\|$. Dividing by $\|g^{\text{mix}}\|$ and using $|A| = \|g_1\| \|g_2\| |\cos \angle(g_1, g_2)|$ yields (20) for a suitable constant C_{rel} . \square

Lemma C.5.1 shows that the PCGrad update is a small perturbation of the mixture gradient whenever the cosine is already close to zero. Combined with Proposition C.3.1, which predicts that A_t (and hence the cosine) decays exponentially under dual-task mixing, this indicates that PCGrad can only have a significant effect during an early transient phase when gradients are strongly conflicting. Once the dynamics enter the near-orthogonal regime, PCGrad and the unmodified dual-task schedule follow almost identical update directions.

Table 6. **Ablation on the reference token.** Adding $\langle \text{CLS} \rangle$ yields improved subject identity scores (CLIP-I, DINO-I) and a higher dynamic degree.

Training Method	Motion Smoothness	Dynamic Degree	CLIP-T	CLIP-I	DINO-I
w/o Ref. token	98.84	54.55	32.87	73.36	57.51
w/ Ref. token	97.99	78.33	33.22	75.87	58.86

Connection to Empirical PCGrad Results. In Sec. B.3 and Fig. 10, we empirically compare gradient alignment with and without PCGrad. Both buffered variants of PCGrad quickly drive the cosine into a narrow band near zero and then track the unprojected dual-task curve closely, which is consistent with Lemma C.5.1 and Proposition C.3.1. Because our stochastic dual-task schedule already reduces gradient conflict rapidly and updates are confined to a low-rank LoRA subspace, the additional projections performed by PCGrad mainly act as a small early-time correction and yield only marginal gains in downstream metrics (Table 5). This theoretical picture supports our choice to adopt the simpler stochastic schedule without PCGrad as the default training recipe.

D. Training Strategies & Ablation Studies

In this section, we present extensive ablation studies on training strategies and various techniques used. Due to the cost of training, we use the model trained with a subset of 4K for paired subject-images [44], since they tend to converge a little faster for the comparison in this section, with less degraded performance according to the Table 4 in the main manuscript, and Sec. D.4.

D.1. Effect of the Reference Token

Tab. 6 demonstrates how adding a dedicated $\langle \text{CLS} \rangle$ token to the prompt affects our model’s performance. Without this reference token, the model attains slightly higher motion smoothness and marginally better CLIP-T scores, but it under-performs on dynamic degree and identity-focused metrics. Introducing $\langle \text{CLS} \rangle$ evidently improves subject fidelity and fosters more diverse motion. We attribute these gains to the reference token guiding the alignment of subject tokens (\mathbf{X}_{in}) with the textual prompt more explicitly, leading to stronger identity preservation and more coherent motion variations.

D.2. T2V vs. I2V Fine-tuning

We also ablate replacing our *image-to-video* (I2V) fine-tuning with a text-to-video (T2V) setup. In Tab. 8, the T2I+T2V (joint) attains a slightly better CLIP-T but lower dynamic degree and subject alignment (CLIP-I, DINO-I). This suggests that T2V fine-tuning struggles when introducing a novel subject identity solely through text, resulting in weaker overall identity preservation. By contrast, our I2V approach strikes a better balance, preserving subject details (CLIP-I: 73.70, DINO-I: 59.29) and maintaining sufficient motion (dynamic degree: 60.19).

D.3. Effect of Varying the Video Dataset Size

Tab. 8 reports how our method’s performance changes when using different amounts of unpaired videos for I2V fine-tuning (1K,

Table 7. Comparison with T2V-only stochastically-switched finetuning, with image drop probability of 1. Switching to text-only input (T2V) moderately boosts CLIP-T but hurts subject fidelity and dynamic degree.

Training Method	Motion Smoothness	Dynamic Degree	CLIP-T	CLIP-I	DINO-I
T2I + T2V (joint)	98.85	44.14	33.41	72.71	48.68
Ours	97.99	78.33	33.22	75.87	58.86

Table 8. Ablation study on using a different number of videos.

Video Count	Motion Smoothness	Dynamic Degree	CLIP-T	CLIP-I	DINO-I
1K	99.03	59.66	32.16	72.69	56.98
2K	98.96	52.25	32.49	72.13	54.42
3K	98.79	55.46	32.04	72.79	55.57
4K	97.99	78.33	33.22	75.87	58.86

2K, 3K, and 4K videos). Notably, with only 1K videos, we already obtain relatively strong results, suggesting that even a small unlabeled corpus can restore temporal consistency to some extent. However, increasing the video count to 4K (our default setting) steadily improves dynamic degree from 59.66 to 78.33 and also boosts identity fidelity (DINO-I) from 56.98 up to 58.56, indicating more consistent subject representation across frames.

We also observe a modest variation in CLIP-T and CLIP-I scores when moving from 1K to 4K videos, suggesting that a larger video dataset helps balance the preservation of subject detail and temporal motion, without overfitting to specific frames or motion patterns. In short, while our method is fairly robust to smaller unlabeled datasets, using around 4K (*i.e.*, 1% of Pexels [29] dataset) videos offers the best trade-off between data efficiency and stable motion/appearance results.

D.4. Effect of Varying the Image Dataset Size

Figure 11 visualizes the qualitative trend when we subsample the S&I corpus from 200K down to 4K and 2K pairs, complementing the VBench summary in Table 4. Consistent with the main paper, using only 4K paired subject-images (about 2% of Subject200K) preserves subject identity convincingly across diverse prompts while maintaining strong motion, as reflected in the 4K results showcased in Fig. 1 and Fig. 6. When further reducing to 2K pairs (about 1%), typical cases still generate with good fidelity and temporal coherence, but occasional failures appear, most notably for small or partially occluded subjects and for fine-grained appearance details, which aligns with the moderate drops in CLIP-I and DINO-I while motion smoothness and dynamic degree remain high in Table 4. These observations support the conclusion that a relatively small subset of paired subject-images can enable identity injection.

D.5. Effect of Varying the Switching Probability

In Tab. 9, we examine how different values of p —the probability of sampling unlabeled video data (I2V fine-tuning)—affect overall performance. When $p = 0.0$, the model relies solely on subject-driven image generation (SDI-Gen) fine-tuning and achieves a rel-

Table 9. Ablation study on using different 'p' to choose I2V finetuning.

Video Ratio	Motion Smoothness	Dynamic Degree	CLIP-T	CLIP-I	DINO-I
0.0	99.60	0.84	32.67	71.15	43.19
0.2 (Ours)	97.99	78.33	33.22	75.7	58.86
0.4	98.31	59.12	31.94	73.53	56.60
0.6	98.33	60.87	31.31	76.71	62.84

atively high dynamic degree but moderate identity scores. Increasing p to 0.2 or 0.4 yields balanced improvements across most metrics, reflecting better coordination between identity and motion. At $p = 0.6$, the model dedicates a greater share of updates to I2V fine-tuning, strengthening identity alignment (CLIP-I: 76.71, DINO-I: 62.84) while keeping the dynamic degree stable (60.87). Although different p values trade off between motion smoothness and identity fidelity to varying degrees, our chosen $p = 0.2$ demonstrates a strong overall balance, as highlighted in the main paper.

D.6. Effect of Random Initial Frame Selection & Dropping.

We further investigate the effects of *random frame selection* and *image-token dropping* during I2V fine-tuning through qualitative analysis. As shown in Figure 12, when neither technique is applied, the first reference image exhibits excessive dominance over subsequent frames, resulting in limited temporal variation. Enabling *random frame selection* alone partially restores temporal dynamics, yet introduces visual artifacts in certain regions (*e.g.*, shirts, oranges). In contrast, the joint application of both techniques achieves a more favorable balance: artifacts are substantially reduced while the reference image blends more naturally into the generated sequence. These qualitative observations underscore the importance of mitigating over-reliance on the first frame and preventing excessive conditioning on a single reference image to achieve smoother, more temporally coherent video generation.

D.7. Effect of Varying Training Strategies

We conduct an ablation on three training strategies: *image-only*, *two-stage*, and our *alternating* (stochastically switched) approach. Qualitative comparisons in Figure 13 reveal distinct failure modes for each strategy. The *image-only* approach produces videos with minimal subject motion, effectively generating near-static sequences that artificially inflate motion-smoothness metrics while sacrificing temporal dynamics, as demonstrated in Table 3 of the main manuscript. *Two-stage* training, which first fine-tunes on paired subject-images before switching to unpaired videos, introduces pronounced visual artifacts and exhibits catastrophic forgetting of the base model’s text-to-video capability. These artifacts manifest as inconsistent textures and structural distortions that compromise overall video quality, despite preserving certain fine-grained image details. In contrast, our proposed *alternating* strategy successfully navigates these failure modes by interleaving identity injection and motion-aware objectives throughout training. As illustrated in Figure 13, this approach generates videos with both natural motion dynamics and coherent visual appear-



Figure 11. Ablation on varying S&I set size used for training. Up to a subset count of 4K, they exhibit successful identity, but when reduced to 2K ($\approx 1\%$ of Subject200K), they show failure from time to time.



Figure 12. Effect of random initial frame and image token dropping.

ance, avoiding the static collapse observed in image-only training and the artifact accumulation in two-stage training. The qualitative results demonstrate that stochastic alternation between objectives effectively maintains the model’s generative capabilities across both modalities.

E. Additional Evaluation

E.1. Human Preference Study

While benchmark metrics offer quantitative insights, they can sometimes be misled by “cheating” behaviors, such as static outputs that yield artificially high scores. To complement our objective measurements, we conducted a human preference study using 20 randomly chosen samples from each baseline and our approach, *without cherry-picking*. A total of 30 participants were asked to rate the generated videos on a five-point Likert scale across dimensions of ID consistency, Prompt alignment, Motion quality,

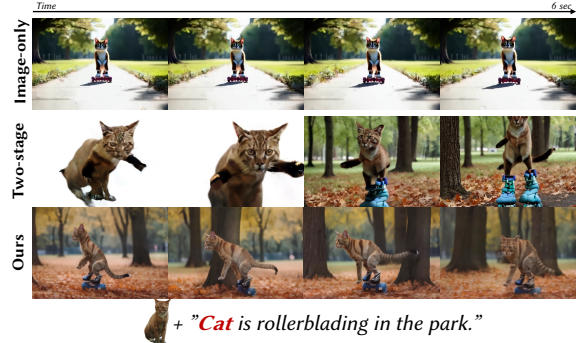


Figure 13. Qualitative result on ablation study of our component in temporal awareness preservation.

Table 10. Result on human preference study in Likert scale of 1-5.

Method	ID Consistency	Prompt Alignment	Motion Quality	Overall Quality
Omini+I2V	3.80	3.78	3.62	3.44
VideoBooth	3.25	3.20	3.08	2.91
Vidu 2.0	3.42	3.24	3.22	3.03
Ours	4.08	3.82	3.88	3.71

and Overall visual appeal. Our method consistently outperformed the baselines, suggesting that our balanced approach to identity preservation and temporal awareness best aligns with human judgments of video realism and quality when viewed holistically.

E.2. Temporal Modeling Evaluation

We evaluate temporal modeling performance using videos sampled from the Pexels dataset, ensuring no overlap with those used during training. Following the protocol of FloVD [28], we categorize videos into three groups based on optical flow magnitude

Table 11. **Temporal Evaluation following FloVD [28], assessing whether motion dynamics improve compared to image-only or two-stage training.** Small - Medium - Large - with each number representing FVD. † denotes Pexels [29]-finetuned version of CogVideoX [54].

Method	Small↓	Medium↓	Large↓
CogVideoX-T2V†	597.54	594.26	573.86
Image-only	641.92	636.42	680.34
Two-stage	801.97	872.30	824.03
Ours	512.30	511.66	550.14

(small: ≤ 25 , medium: $25 \sim 50$, large: ≥ 50) to enable detailed analysis. For object-motion evaluation in particular, we focus on videos with minimal or no camera motion and construct benchmark subsets by applying the same motion-based grouping to a separate collection of Pexels videos not used in our stochastically switched fine-tuning.

E.2.1. Evaluation Protocol

1) Foreground–Background Segmentation. For each video, we use an off-the-shelf segmentation model (e.g., Grounded-SAM2) on the *first frame* to separate foreground and background regions. This allows us to measure object (foreground) motion independently from any camera-induced background shifts.

2) Optical Flow Computation. We estimate optical flow between the *first frame* and each subsequent frame using a standard flow estimator (e.g., RAFT [45]). Let $\mathbf{u}_f(x)$ and $\mathbf{u}_b(x)$ denote the per-pixel flow vectors for the foreground and background pixels, respectively, at position x . We record:

$$\text{FlowMag}_f = \frac{1}{N_f} \sum_{x \in \text{fg}} \|\mathbf{u}_f(x)\|,$$

$$\text{FlowMag}_b = \frac{1}{N_b} \sum_{x \in \text{bg}} \|\mathbf{u}_b(x)\|,$$

where N_f and N_b are the respective pixel counts in the foreground and background masks.

3) Dataset Filtering. To ensure negligible camera motion, we *discard* any video whose average magnitude of background flow FlowMag_b exceeds 10 pixels. This filtering step excludes scenes with significant global shifts, retaining only those with primarily object-centric motion.

4) Category Assignment. Based on the average magnitude of foreground flow FlowMag_f (averaged over all frames), we categorize videos into:

- *Small*: $0 \leq \text{FlowMag}_f \leq 25$
- *Medium*: $25 < \text{FlowMag}_f \leq 50$
- *Large*: $\text{FlowMag}_f > 50$

Each category contains 300 videos, ensuring a balanced evaluation of low-, moderate-, and high-motion scenarios.

5) Evaluation Protocol. Within each subset, we use only the *first frame* (including any textual or reference cues, if required) to generate a video of the same length. We then compute FVD [32] between the generated outputs and the ground-truth videos. By comparing FVD across *small*, *medium*, and *large* motion classes, we obtain a clearer picture of how each model (ours vs. baselines) adapts to varying object-motion intensities.

E.2.2. Discussion.

We compared *image-only*, *two-stage*, and our *dual-task learning* strategies. Image-only training produced a video with poor FVD (Tab. 11). Two-stage fine-tuning leads to high FVD, which aligns with the result of artifacts as in Fig. 13. Our strategy (Ours) excelled, with lower FVD scores confirming superior motion realism and temporal consistency, on par with CogVideoX [54].

One thing to note is that motion-focused split highlights each method’s strengths and weaknesses. For example, a model might produce near-static outputs for low-motion data, *cheating* on metrics such as smoothness in VBench metrics, yet fail to track fast-moving objects in high-motion videos. As observed in FloVD [28], categorizing by foreground flow magnitude reveals these nuances more effectively than aggregated scores alone.

Additional Details. To ensure a fair comparison with our method, we additionally fine-tune the original CogVideoX [54] on a subset of the Pexels [29] dataset that is equivalent to the one used in our training. Since our model is trained for 4K steps with a sampling ratio $p = 0.2$, we match this by finetuning CogVideoX for 800 steps (0.2×4000). As a result, we achieved performance comparable to the original CogVideoX in motion dynamics evaluation.

E.3. Evaluation on Other Benchmark

We evaluate the proposed zero-shot SDV-Gen model on the Open S2V [58] Evaluation Benchmark (single-domain track) without any per-subject tuning or domain-specific adaptation, using the same checkpoint trained on 200K paired subject-images and 4K unpaired videos described in the main paper. Table 12 summarizes the quantitative results and training cost. Our method attains a total Score of **50.05%**, comparable to Phantom-1.3B (49.95%) and within range of recent closed models, while requiring only **288 A100-hours** of fine-tuning. Metric-wise, our model achieves the *highest* GmeScore at **70.53%**, strong Aesthetics at **45.40%** (second only to Phantom-14B at 47.46%), and a competitive NaturalScore of **68.52%**, indicating that the paired subject-images coupled with unpaired videos preserve visual appeal and realism despite the small compute budget.

The Motion score (**19.38%**) lags behind larger video-centric models such as Phantom-14B (41.55%) and Kling-1.6 (36.40%), consistent with our compute-efficient training that predominantly optimizes on images and conservatively preserves motion priors rather than aggressively amplifying motion. FaceSim is also lower (**18.05%**) than face-specialized or video-heavy models, aligning with our limitation analysis that Subject-200K contains almost no human faces and that our training does not include a face-focused identity corpus. However, it is similar to that of Phantom-1.3B or VACE-P1.3B or SkyReels-A2-P14B, demonstrating similar performance. (See supplement video for examples on facial identities.)

In terms of efficiency, our 288 A100-hours constitute roughly $35\text{--}104\times$ lower cost than Phantom-1.3B/14B ($(\approx)10\text{K--}30\text{K}$ hours) and $240\text{--}730\times$ lower than VACE-1.3B/14B ($(\approx)70\text{K--}210\text{K}$ hours), yet yield comparable Total Score to several baselines. Overall, these results indicate that a zero-shot SDV-Gen model trained mostly on paired subject-images can compete on the Open S2V single-domain track with orders of magnitude less compute.

Table 12. **Quantitative comparison among different methods for the single-domain subject-to-video task along with Training Cost in A100 GPU hours.** Total score is the normalized weighted sum of other scores and “↑”, higher is better.

Method	Training Cost	Total Score↑	Aesthetics↑	Motion↑	FaceSim↑	GmeScore↑	NexusScore↑	NaturalScore↑
Vidu2.0	-	48.67%	34.78%	24.40%	36.20%	65.56%	45.20%	72.60%
Pika2.1	-	48.93%	38.64%	31.90%	32.94%	62.19%	47.34%	70.60%
Kling1.6	-	53.12%	35.63%	36.40%	39.26%	61.99%	48.24%	81.40%
VACE-P1.3B	≈70K hours	44.28%	42.58%	18.00%	18.02%	65.93%	36.26%	76.00%
VACE-1.3B	≈70K hours	47.33%	41.81%	33.78%	22.38%	65.35%	38.52%	76.00%
VACE-14B	≈210K hours	58.00%	41.30%	35.54%	64.65%	58.55%	51.33%	77.33%
Phantom-1.3B	≈10K hours	49.95%	42.98%	19.30%	44.03%	65.61%	37.78%	76.00%
Phantom-14B	≈30K hours	53.17%	47.46%	41.55%	51.82%	70.07%	35.35%	69.35%
SkyReels-A2-P14B	-	51.64%	33.83%	21.60%	54.42%	61.93%	48.63%	70.60%
HunyuanCustom	-	51.64%	34.08%	26.83%	55.93%	54.31%	50.75%	68.66%
Ours	288 hours	50.05%	45.40%	19.38%	18.05%	70.53%	41.23%	68.52%

F. Estimation of Other Methods’ Training Cost

We estimate the train time of CustomCrafter [53] and VACE [27] based on the given implementation details in the manuscript.

F.1. CustomCrafter.

The estimated GPU hours for training a single subject are in the range of 100–300 A100-hours, with a median estimate of around 200 A100-hours.

$$\text{wall-clock time (hours)} = \frac{10\,000 \times t}{3\,600}$$

$$\text{total GPU-hours} = 4 \times \text{wall-clock time}$$

where $t \in [10, 30]$ is the estimated time per iteration in seconds.

F.2. VACE.

The estimated GPU hours for training VACE on LTX-Video are in the range of 9,000–27,000 A100-hours, with a median estimate of around 18,000 A100-hours.

$$\text{number of training steps} = 200\,000$$

$$\text{wall-clock time per training (hours)} = \frac{200\,000 \times t}{3\,600}$$

$$\text{GPU-hours} = 16 \times \frac{200\,000 \times t}{3\,600} = \frac{3\,200\,000t}{3\,600} = \frac{8\,000t}{9}$$

where $t \in [10, 30]$ is the estimated time per iteration in seconds. The estimated GPU hours for training VACE on Wan-T2V are in the range of 70,000–210,000 A100-hours, with a median estimate of around 140,000 A100-hours.

$$\text{number of training steps} = 200\,000$$

$$\text{wall-clock time per training (hours)} = \frac{200\,000 \times t}{3\,600}$$

$$\text{GPU-hours} = 128 \times \frac{200\,000 \times t}{3\,600} = \frac{25\,600\,000t}{3\,600} = \frac{64\,000t}{9}$$

where $t \in [10, 30]$ is the estimated time per iteration in seconds.

F.3. VideoBooth.

VideoBooth trains two stages (coarse and fine), each for 218,000 steps, totaling 436,000 training steps. We estimate the total compute assuming an $8 \times \text{A100}$ setup.

$$\text{number of training steps} = 218,000 + 218,000 = 436,000$$

$$\text{wall-clock time per training (hours)} = \frac{436,000 \times t}{3,600}$$

$$\text{GPU-hours} = 8 \times \frac{436,000 \times t}{3,600} = \frac{3,488,000t}{3,600} = \frac{8,720t}{9}$$

where $t \in [0.8, 2.0]$ is the estimated time per iteration in seconds.

Therefore, the estimated GPU hours for training VideoBooth are in the range of 775–1,938 A100-hours, with a median estimate of around 1,356 A100-hours (at $t = 1.4$).

G. Additional Qualitative Result

We showcase the qualitative result with comparison to the per-subject tuning baselines in Figs. 14, 15 and zero-shot baselines in Figs. 16, 17, including state-of-the-art models [27, 33]. To compare, we use Phantom-Wan 2.1-1.3B and VACE-Wan 2.1-1.3B for comparison. Note that *mini* denotes our model that is trained with a 4,000-subset of paired subject-images [44].

We demonstrate additional qualitative video results in the supplemental video and include Open-S2V-Evaluation [58] Benchmark results in the supplemental video.

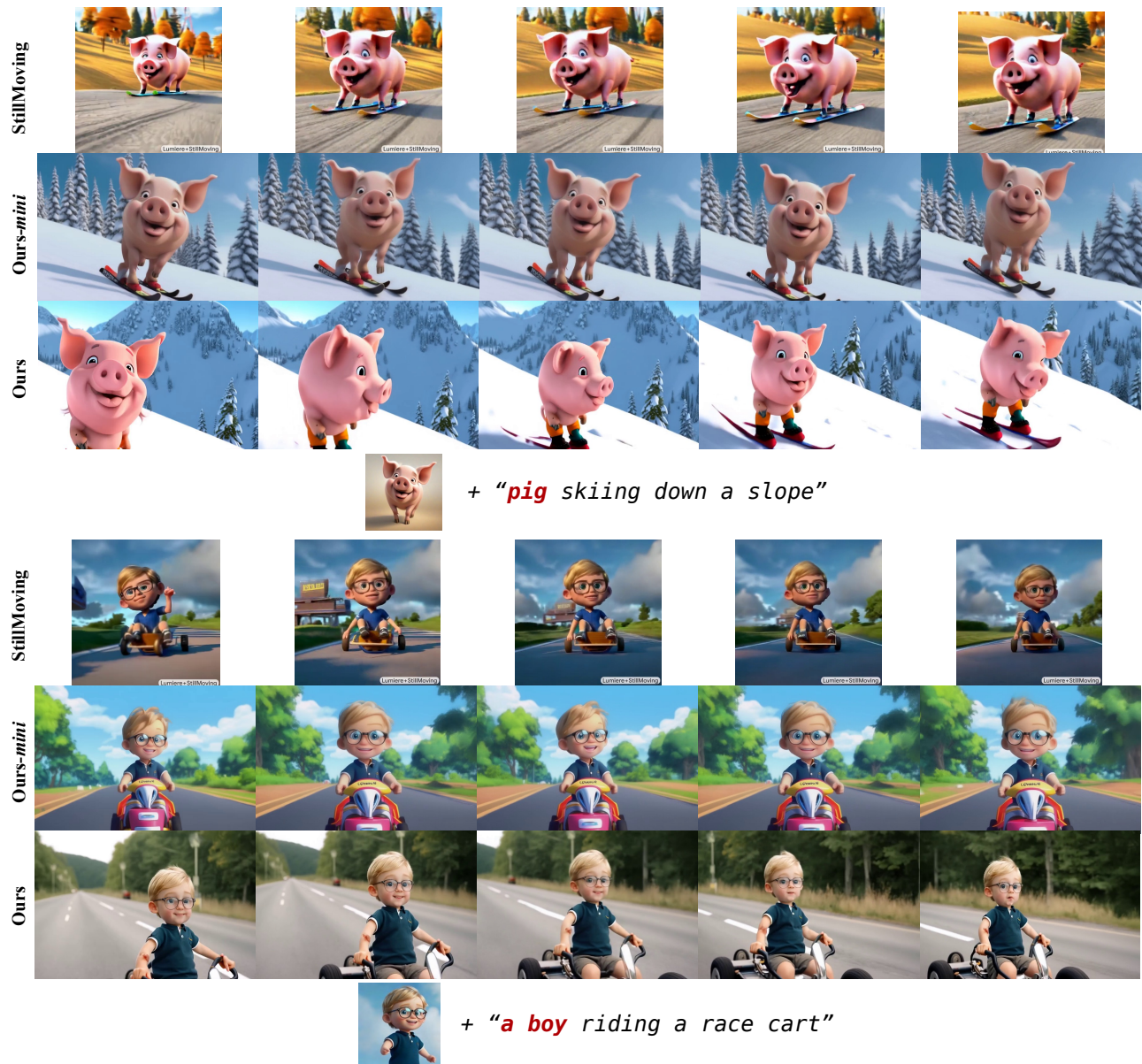


Figure 14. Additional qualitative comparison with Still-Moving [7]. Note that *mini* denotes our method trained with a 4K subset of Subject 200K [44].



+ *"a teddy bear is playing guitar"*



+ *"anime girl selfie standing under the pink blossoms of a cherry tree"*

Figure 15. Additional qualitative comparison with CustomCrafter [53]. Note that *mini* denotes our method trained with 4K subset of Subject 200K [44].



+ "Under the glow of a streetlamp, a toy car comes closer to camera on a wet pavement, reflecting the flickering city lights."

Figure 16. Additional qualitative comparison with tuning-free baselines including VACE Wan-1.3B [27], Phantom Wan-1.3B [33]. Note that *mini* denotes our method trained with 4K subset of Subject 200K [44]

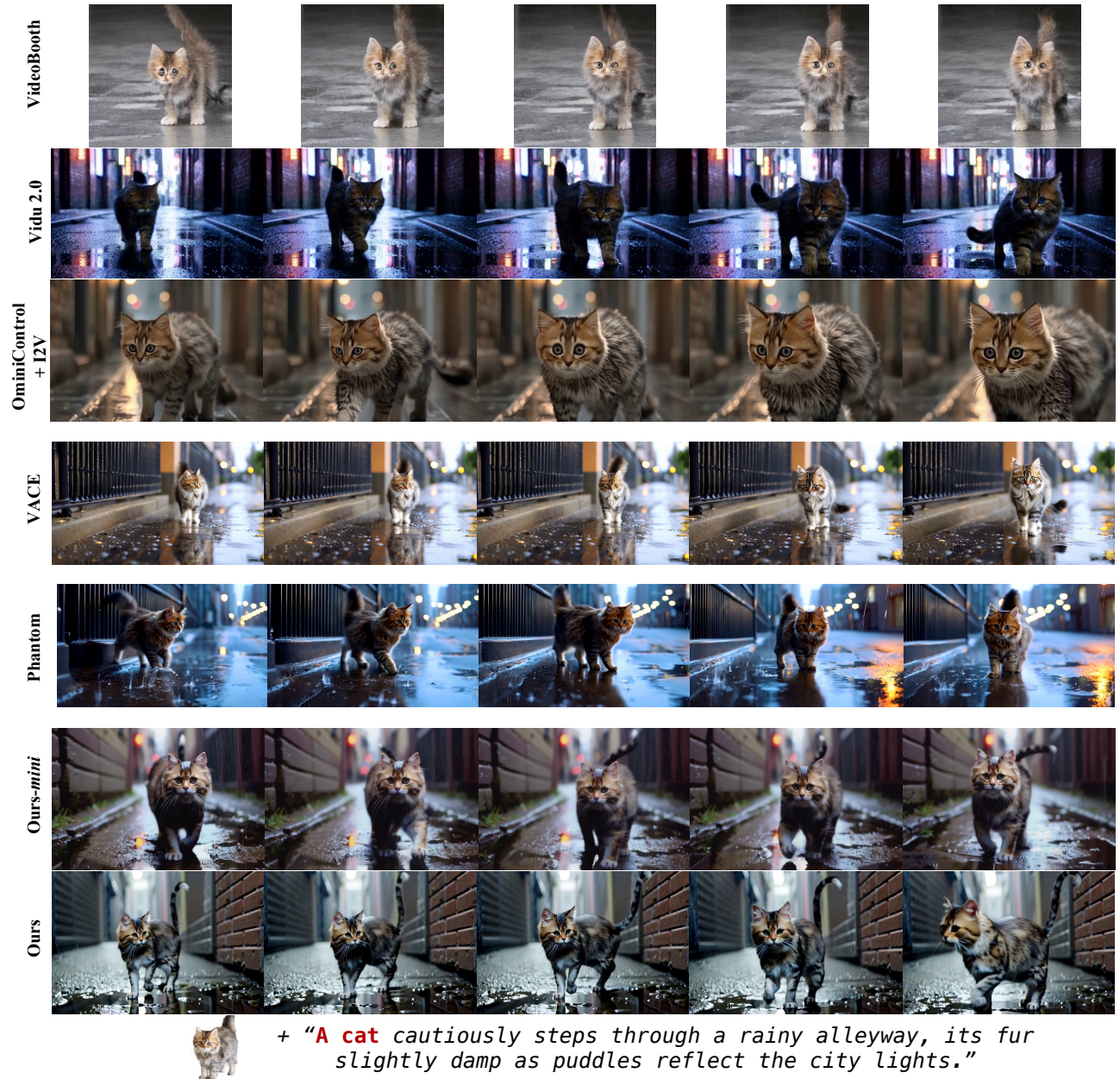


Figure 17. Additional qualitative comparison with tuning-free baselines including VACE Wan-1.3B [27], Phantom Wan-1.3B [33]. Note that *mini* denotes our method trained with 4K subset of Subject 200K [44]